

THE 37-MONTH MAXI/GSC SOURCE CATALOG IN THE HIGH GALACTIC-LATITUDE SKY

KAZUO HIROI,¹ YOSHIHIRO UEDA,¹ MASAAKI HAYASHIDA,¹ MEGUMI SHIDATSU,¹ RYOSUKE SATO,¹ TAIKI KAWAMURO,¹ MUTSUMI SUGIZAKI,² SATOSHI NAKAHIRA,³ MOTOKO SERINO,² NOBUYUKI KAWAI,⁴ MASARU MATSUOKA,^{2,3} TATEHIRO MIHARA,² MIKIO MORII,⁴ MOTOKI NAKAJIMA,⁵ HITOSHI NEGORO,⁶ TAKANORI SAKAMOTO,⁷ HIROSHI TOMIDA,³ YOHKO TSUBOI,⁸ HIROSHI TSUNEMI,⁹ SHIRO UENO,³ KAZUTAKA YAMAOKA,¹⁰ ATSUMASA YOSHIDA,⁷ MASATO ASADA,⁶ SATOSHI EGUCHI,¹¹ TAKANORI HANAYAMA,¹² MASAYA HIGA,⁸ KAZUTO ISHIKAWA,⁴ MASAKI ISHIKAWA,¹³ NAOKI ISOBE,¹⁴ MITSUHIRO KOHAMA,¹⁵ MASASHI KIMURA,³ KUMIKO MORIHANA,² YUJIN E. NAKAGAWA,¹⁴ YUKI NAKANO,⁷ YASUNORI NISHIMURA,¹² YUJI OGAWA,¹² MASAYUKI SASAKI,⁹ JURI SUGIMOTO,² TOSHIHIRO TAKAGI,² RYUICHI USUI,⁴ TAKAYUKI YAMAMOTO,² MAKOTO YAMAUCHI,¹² AND KOSHIRO YOSHIDOME¹²

Accepted on August 17, 2012

ABSTRACT

We present the catalog of high Galactic-latitude ($|b| > 10^\circ$) X-ray sources detected in the first 37-month data of Monitor of All-sky X-ray Image (MAXI) / Gas Slit Camera (GSC). To achieve the best sensitivity, we develop a background model of the GSC that well reproduces the data based on the detailed on-board calibration. Source detection is performed through image fit with the Poisson likelihood algorithm. The catalog contains 500 objects detected in the 4–10 keV band with significance of $s_{D,4-10\text{keV}} \geq 7$. The limiting sensitivity is $\approx 7.5 \times 10^{-12} \text{ ergs cm}^{-2} \text{ s}^{-1}$ ($\approx 0.6 \text{ mCrab}$) in the 4–10 keV band for 50% of the survey area, which is the highest ever achieved as an all-sky survey mission covering this energy band. We summarize the statistical properties of the catalog and results from cross matching with the Swift/BAT 70-month catalog, the meta-catalog of X-ray detected clusters of galaxies, and the MAXI/GSC 7-month catalog. Our catalog lists the source name (2MAXI), position and its error, detection significances and fluxes in the 4–10 keV and 3–4 keV bands, their hardness ratio, and basic information of the likely counterpart available for 296 sources.

Subject headings: catalogs — surveys — galaxies: active — X-rays: galaxies

1. INTRODUCTION

Monitor of All-sky X-ray Image (MAXI: Matsuoka et al. 2009) is the first astronomical mission performed on the International Space Station (ISS). The main instrument of MAXI is the Gas Slit Camera (GSC: Mihara et al. 2011; Sugizaki et

Electronic address: hiroi@kusastro.kyoto-u.ac.jp

¹ Department of Astronomy, Kyoto University, Oiwake-cho, Sakyo-ku, Kyoto 606-8502

² MAXI team, Institute of Physical and Chemical Research (RIKEN), 2-1 Hirosawa, Wako, Saitama 351-0198

³ ISS Science Project Office, Institute of Space and Astronautical Science (ISAS), Japan Aerospace Exploration Agency (JAXA), 2-1-1 Sengen, Tsukuba, Ibaraki 305-8505

⁴ Department of Physics, Tokyo Institute of Technology, 2-12-1 Ookayama, Meguro-ku, Tokyo 152-8551

⁵ School of Dentistry at Matsudo, Nihon University, 2-870-1 Sakaecho-nishi, Matsudo, Chiba 201-8308

⁶ Department of Physics, Nihon University, 1-8-14 Kanda-Surugadai, Chiyoda-ku, Tokyo 101-8308

⁷ Department of Physics and Mathematics, Aoyama Gakuin University, 5-10-1 Fuchinobe, Chuo-ku, Sagamihara, Kanagawa 252-5258

⁸ Department of Physics, Chuo University, 1-13-27 Kasuga, Bunkyo-ku, Tokyo 112-8551

⁹ Department of Earth and Space Science, Osaka University, 1-1 Machikaneyama, Toyonaka, Osaka 560-0043

¹⁰ Astro-H Project team, Institute of Space and Astronautical Science (ISAS), Japan Aerospace Exploration Agency (JAXA), 3-1-1 Yoshino-dai, Chuo-ku, Sagamihara, Kanagawa 252-5210

¹¹ National Astronomical Observatory of Japan, 2-21-1, Osawa, Mitaka City, Tokyo 181-8588

¹² Department of Applied Physics, University of Miyazaki, 1-1 Gakuen Kibanadai-nishi, Miyazaki, Miyazaki 889-2192

¹³ School of Physical Science, Space and Astronautical Science, The graduate University for Advanced Studies (Sokendai), Yoshinodai 3-1-1, Chuo-ku, Sagamihara, Kanagawa 252-5210

¹⁴ Institute of Space and Astronautical Science (ISAS), Japan Aerospace Exploration Agency (JAXA), 3-1-1 Yoshino-dai, Chuo-ku, Sagamihara, Kanagawa 252-5210

¹⁵ Mitsubishi Space Software Co., Ltd., WTC Bldg.2-4-1 Hamamatsu-cho, Minato-ku, Tokyo 105-6132

al. 2011), which covers the 2–30 keV band. Since its first light on 2009 August 15, MAXI/GSC has been monitoring nearly the entire sky every 92 minute with two instantaneous field-of-views of $1.5^\circ \times 160^\circ$ that rotate according to the orbital motion of the ISS. The survey with MAXI/GSC is expected to achieve the best sensitivity so far as an all-sky monitor in the 2–10 keV band, which is complementary to other all-sky surveys conducted below 2 keV (ROSAT: Voges et al. 1999, 2000) and above 10 keV (INTEGRAL: Bird et al. 2007; Beckmann et al. 2006, 2009; Krivonos et al. 2007; Bird et al. 2010, Swift: Tueller et al. 2008, 2010; Cusumano et al. 2010; Baumgartner et al. 2010, 2012). This bandpass is the most suitable to survey X-ray populations with intrinsically soft X-ray spectra with little bias for obscuration.

Utilizing the first 7-month data of MAXI/GSC in the 4–10 keV band, Hiroi et al. (2011) produced the first X-ray source catalog in the high Galactic latitude sky ($|b| > 10^\circ$). It consists of 143 objects above the 7σ significance level with a limiting sensitivity of $\sim 1.5 \times 10^{-11} \text{ ergs cm}^{-2} \text{ s}^{-1}$ (1.2 mCrab) in the 4–10 keV band. Though limited in sample size, the first MAXI/GSC catalog has an advantage that the identification completeness is very high ($> 99\%$). Utilizing the AGN sample of this catalog, Ueda et al. (2011) calculate a new AGN X-ray luminosity function in the local universe and solve the discrepancy of the AGN space density previously reported from different missions.

In this paper, we present the second MAXI/GSC source catalog at $|b| > 10^\circ$, constructed from the data in the 4–10 keV band observed for 37 months between 2009 September and 2012 October. The significantly increased photon statistics enables us to achieve much better sensitivities than those of the 7-month catalog. We also analyze the data in the 3–4 keV band to derive the hardness ratio of the detected sources. Section 2 describes the data reduction and filtering. In section 3, we report the analysis procedures to detect source candidates and determine their fluxes and positions. Section 4 presents

the source catalog, its basic properties, the results from cross-matching with other X-ray source catalogs, and the log N -log S relation. We summarize our conclusion in section 5.

2. DATA REDUCTION

The second MAXI/GSC catalog is based on the 37-month data obtained from 2009 September 23 to 2012 October 15. The data reduction procedure is essentially the same as used to produce the MAXI/GSC 7-month catalog in Hiroi et al. (2011). We start from processed event files provided by the MAXI team, which have columns of the photon arrival time (TIME), energy (Pulse-height Invariant = PI), and sky position (R.A. and Decl.). In the processing, two pulse-height values read out from both ends of a carbon-anode wire were converted into the PI and an one-dimensional detector position along the anode wire on the basis of the ground and in-flight calibration (Mihara et al. 2011; Sugizaki et al. 2011). The sky position of the incident X-ray photon is then calculated by referring to the ISS attitude at the photon arrival time. For the data reduction, we use HEAsoft (version 6.12) and MXSOFT, an original MAXI software package developed by the MAXI team.

To detect sources, the data in the 4–10 keV band are utilized for consistency with our previous work (Hiroi et al. 2011), where high signal-to-noise ratio is achievable due to the high quantum efficiency and low background rate of the detector (Mihara et al. 2011). We basically use all available data of all twelve GSC counters operated with high voltage levels of both 1650 V and 1550 V, except for those taken with GSC_3 after 2010 June 22, in which the background-veto counters were not available. Unlike Hiroi et al. (2011), the photon events of anode #1 and #2 are also available in this study, thanks to the improvement of the instrument response calibration. We discard the data acquired in unusual conditions where the background reproducibility of the GSC is found to be poor: (1) the initial operation phase from 2009 September 1 to 22, (2) the phase from 2012 October 16 to 31 when the Dragon spacecraft was attached to the ISS, (3) those during the docking or undocking operation of the Soyuz spacecraft, (4) those soon after the reboot of the electrical system of MAXI, (5) those during large solar flares¹⁶, and (6) those when the telemetry data were missed due to the network trouble between the ISS and the ground base station.

The following data selection criteria are applied in event selection. To exclude data of the GSC with high particle background, we select the events when the latitude of the ISS is between -40° and 40° and those detected in an inner region of each camera with the incident angle $|\phi| \leq 38^\circ$ (for definition of ϕ , see Mihara et al. 2011). In our new analysis for the 37-month catalog, we also properly take into account the effects of the occultation of the GSC field-of-views by the space shuttle and the solar paddles of the ISS in a time dependent manner; the occulted regions in the detector coordinate defined by ϕ at a given time, if any, are excluded with a margin of 5° on the basis of monitoring information of the relative geometry between MAXI and the ISS.

The left panel of figure 1 displays the effective exposure map for the 37-month MAXI/GSC data in the Galactic coordinates projected with the Hammer-Aitoff algorithm. The effective-exposure distribution is shown in the right panel.

¹⁶ From the light curves with 16-sec bin size in the 4–10 keV band, we filter out time regions when the count rates exceeded 25, 35, 40, and 30 cnts/s for GSC_3, GSC_8, GSC_B, and the other cameras, respectively, with margins of 32 sec each before and after these periods.

The map is produced by the latest version of the MAXI simulator **maxisim** (Eguchi et al. 2009) for uniformly extended emission, where the ϕ dependence of the slit area, the collimator field-of-view, and the detector efficiency as a function of an incident X-ray energy (see Mihara et al. 2011; Sugizaki et al. 2011) are correctly taken into account. Referring to the orbit and attitude of the ISS, **maxisim** is able to generate simulated photon events from any input X-ray sources by reflecting the latest responses of the GSC. The stripe patterns found in the map are caused by an incident-angle dependence of the effective area of the GSC aimed at each pointing direction, the different duty cycle among the twelve GSC counters, and the precession of scanning motion of the field-of-views coupled with that of the ISS orbit. The two darkest, annular-like structures at the top-left and bottom-right of the map correspond to the regions with the longest exposure near the poles around the rotation axis of the ISS orbit.

3. ANALYSIS

3.1. Background Reproduction

For source detection, we perform image analysis of the projected sky image from the whole MAXI/GSC data, as detailed in section 3.2. Basically, we search for excess signals over the profile of the background, which consists of the non-X-ray background (NXB) and the cosmic X-ray background (CXB). Thus, to achieve the best sensitivity, it is critical to model the background image with the least systematic errors that enables us to detect even the faintest sources as statistically significant signals. The NXB of the GSC shows complex behaviors (Sugizaki et al. 2011). The rate of the NXB is highly variable, depending on the environment such as conditions of other spacecrafats attached to the ISS, the orbital position and attitude of the ISS.

We thus construct a background model of MAXI/GSC based on the detailed calibration of the on-board data as described below. Here we do not distinguish the NXB from the CXB, only treating their sum, since it is not easy to separate the two components from the observed data. This is mainly due to the fact that the MAXI/GSC field-of-views always look at the sky and seldom look at the earth. For this purpose, we analyze the on-board data that can be regarded as blank sky, by excluding regions around the 70 brightest sources at high Galactic latitudes listed in the 7-month MAXI/GSC catalog¹⁷ (Hiroi et al. 2011) and that of the Galactic-center region with $|l| < 50^\circ$ and $|b| < 10^\circ$. The same screening described in section 2 is adopted for event extraction. To avoid complexity in exposure correction, we discard any data taken when a part of the field-of-view was occulted by the space shuttle and the solar paddles of the ISS in each camera.

We first investigate the long-term variability of the background rate. The top panel of figure 2 displays a one-day averaged background rate as a function of time, derived from the data in the 4–10 keV band taken with the GSC_4 counter. It is clearly seen that the MAXI/GSC background rate has two separate levels of 3–4 cnts/s and 2–2.5 cnts/s in this camera. We find that this long-term variability of the background is strongly correlated with whether the Soyuz spacecraft was docked or undocked to the ISS. Since Soyuz has an altimeter containing a radioactive source, the MAXI/GSC background rate is largely increased when it is attached to the nearest ISS

¹⁷ We confirm that when our new 37-month catalog is used to exclude even fainter sources in this process, the resultant background profile in the detector coordinate is little ($< 1\%$) changed.

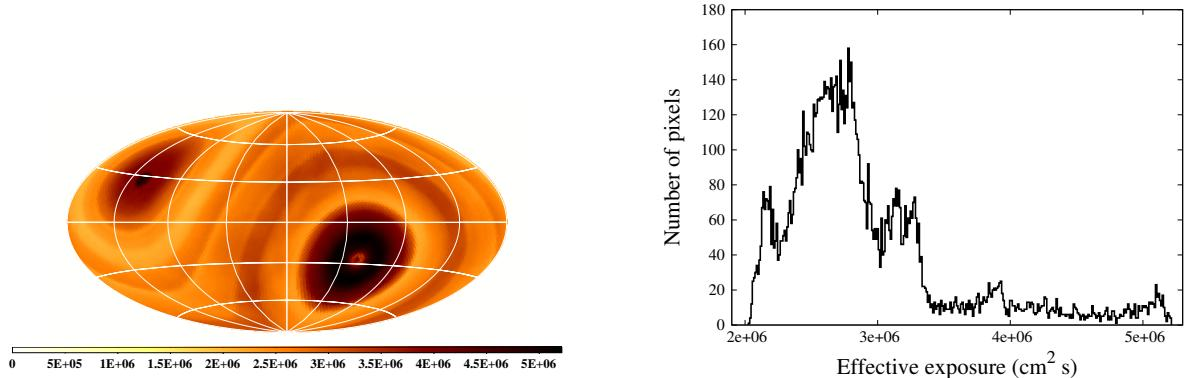


FIG. 1.— (Left) Effective exposure map for the 37-month MAXI/GSC data in the Galactic coordinates projected with the Hammer-Aitoff algorithm. The units are cm² s. The entire sky is divided into 12288 pixels with a size of 1.83° × 1.83°. (Right) Histogram of the effective exposure presented in the left panel.

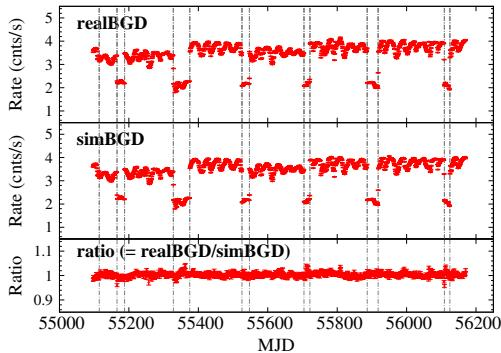


FIG. 2.— (Top) History of the background rate in the 4–10 keV band observed with GSC_4 in a one-day bin (real data). The attached error is 1σ . The dot-dashed lines indicate the boundaries of the phases. The dock/undock status of the Soyuz spacecraft causes the drastic change of the daily background rate. (Middle) Same as the top panel but produced from simulations. (Bottom) The ratio of the real background rate to the simulated one. The simulated background data are well consistent with the real ones with an rms scatter of $\sim 1\%$.

port to MAXI, and vice versa. Furthermore, it is found that an increment of the background rate depends on the individual Soyuz spacecraft docked at that time. The difference of high-voltage level between 1650 V and 1550 V also affects the background rate. Thus, we divide the 37-month period into 9 different phases according to the existence of Soyuz and the high-voltage level of the GSC, and create the background model separately in each phase.

Next, the short-term variability of the NXB on a time scale less than one day is examined. In the previous study (Hiroi et al. 2011), we considered the dependence of the background rate on the cut-off rigidity (COR) parameter, which is determined solely by the orbital position of the ISS. The correlation of the NXB with COR is known to be not so good, however. Alternatively, we have found that the instantaneous background rate is well estimated from the so-called “VC” count, representing the rate of events simultaneously detected by the carbon-anode cells and the tungsten-anode cells for particle veto, available as a monitor count in the house keeping data of the GSC (Mihara et al. 2011; Sugizaki et al. 2011). The reason why the VC works as a good monitor of the NXB is that high energy particles hitting the GSC counter should be detected by both the inner (carbon) and outer (veto) cells, unlike X-ray events. Figure 3 plots examples of the correlation between the VC and background rates in the 4–10 keV band for GSC_4 in two different phases. The blue circles and

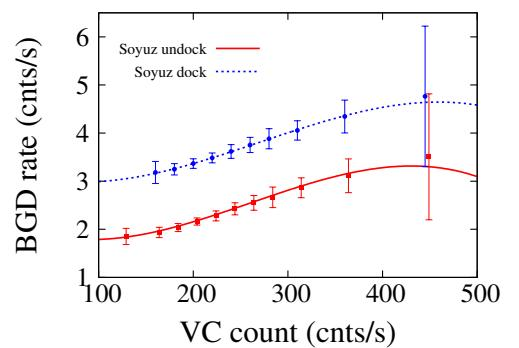


FIG. 3.— Correlation between the 4–10 keV background rate and the VC count rate for GSC_4. The red squares (for visuality, slightly shifted) and solid curve represent the data points and the best-fit model of a third-order polynomial, respectively, when Soyuz was undocked, while the blue circles and dotted curve show them when it was docked from 2009 December 22 to 2010 May 11 (MJD = 55187–55327).

red squares correspond to the data obtained when Soyuz was docked to the ISS port and undocked, respectively. The error bars represent 1σ standard deviation in the background rate including the statistical fluctuation. A tight correlation is confirmed in each phase. The blue-dotted and red-solid lines represent the best-fit models of a third-order polynomial to these correlations.

We develop a background-event generator of the GSC, which makes use of the framework of the MAXI simulator **maxsim**. By using the correlation between the VC and background rates determined for each camera and phase, it generates simulated background events in time series with the instantaneous rate calculated from the light curve of the VC counts. Their energies and positions on the detector are randomly assigned according to their distributions derived from the real background data, which also depend on the VC count. We produce ten times more events than the real data to reduce the statistical error in the model. The simulated background data are then processed in the same way as for the observed data. The middle panel of figure 2 plots the same as that shown in the top panel of figure 2 but based on the simulated background data. We confirm that the background light curve is well reproduced by our model with an rms scatter of $\sim 1\%$, as shown in the bottom panel of figure 2.

3.2. Image Analysis

In this section, we describe the details of our image analysis method to produce the X-ray catalog from the MAXI/GSC

data. The procedure consists of two major stages: a detection of source candidates from smoothed images, and a measurement of fluxes and positions for the source candidates by maximum-likelihood image fitting. For the image analysis, we use *display45* version 2.04, which is a command-driven, interactive histogram-browsing program based on CERN libraries.

(1) MAKING PARTED IMAGES

Both for the real and simulated background data, we create images from the event lists after applying the selection criteria described in section 2. Like a standard image analysis, we produce a tangentially-projected image within a small region in the sky coordinates (X, Y) defined by three parameters: the reference point in right ascension (R.A.) and declination (Decl.) corresponding to the center of the image and the position angle of the + Y -axis to the north, which is set to be zero in our analysis. The images are simply stored in units of counts without exposure correction.

The entire sky is divided into 768 square regions with a size of $7.3^\circ \times 7.3^\circ$, whose centers are determined by using the HEALPix software package (Górski et al. 2005) so that each region has the same solid angle. Using the central position of each region as the sky-reference point, we then make 768 tangentially-projected images with a size of $14^\circ \times 14^\circ$ by referring to the columns of sky position (R.A., Decl.) in the event lists. In order not to miss any sources located near the boundaries, the images have overlapping area of $> 3^\circ$ on both sides with neighboring ones. The bin size is set to 0.1° , which is sufficiently finer than the typical size of the point spread function (PSF) of MAXI/GSC (FWHM $\sim 1.5^\circ$).

(2) SEARCHING FOR SOURCE CANDIDATES

To pick up source candidates from each image, we create a significance map in the following manner. Firstly, we make net-source maps by subtracting the simulated background from the real data. Then, both the real data and net-source map are smoothed with a circle of $r = 1^\circ$ with a constant weight of unity (i.e., simple integration). We finally calculate the significance of excess signals as “net-source/ $\sqrt{\text{real data}}$ ” at each point, yielding the significance map.

In this step, a correct estimate of the background level is essential. Although the reproducibility of the background model described in section 3.1 is fairly good for blank sky, we find that it is sometimes better to re-normalize the absolute level of the background map from the observed data themselves, in particular when additional diffuse background other than the CXB such as Galactic diffuse emission exists in the image. Thus, the background level used to make a final source-candidate list is determined by iteration in the following way. At first, assuming a conservative background level higher than the nominal value by a factor of 1.1, we create a tentative significance map. We then search for the peak showing the highest significance in the map if it is larger than 15σ . Next, after masking out the circular region around the peak of the bright source with a radius of $r = 3^\circ$, the whole size of the PSF, we compare the averaged counts in the real and the simulated background maps, whose ratio determines an improved background level. By repeating these procedures of finding and masking out brightest sources until the significance of a newly detected peak becomes $< 15\sigma$, we finally derive the most reasonable background level in each image. The correction from the nominal level is typically less than 3%, and thus

possible systematic errors in the positional dependence of the background do not affect the flux measurements of sources.

Once the background level is determined, we make the most reliable significance map, from which peaks above 5σ are picked up as source candidates. Those located near the boundaries of the image ($|X| > 5.5^\circ$ or $|Y| > 5.5^\circ$) are discarded because they are located closer to the center of a neighboring image that can detect them with better conditions. The issue of source confusion that two nearby sources may be detected as a single source candidate will be overcome in a later procedure (the 6th step).

(3) MERGING SOURCE-CANDIDATE LIST

Merging the source-candidate lists obtained from the whole sky yields 1308 sources in total above 5σ at $|b| > 10^\circ$. This list includes duplicate sources detected in multiple images, however, which are located at the overlapping regions near the boundaries. We treat any pair of sources whose positions are within 1° as a single object; we adopt a source detected at a closer position to the image center and discard the other. It is confirmed that the detection significances of the paired candidates are consistent with each other within expected levels. Thus, we finally obtain a unique source-candidate list consisting of 615 objects above 5σ at $|b| > 10^\circ$.

(4) CONSTRUCTING MODELS OF POINT SPREAD FUNCTION

For image analysis, we need to construct a model of the PSF for each source candidate. Since the MAXI/GSC data used in this study compose of multiple observations with different conditions, it is difficult to model the PSF shape analytically. Hence, we utilize the MAXI simulator **maxisim** (Eguchi et al. 2009) to produce the PSF model by inputting a point-like source at the detected position. The simulation is performed with exactly the same observational conditions (such as the total exposure) as for the real data, and hence the resultant PSF contains the expected number of counts from that source with a given flux by fully taking into account the instrumental responses. The Crab Nebula-like spectrum¹⁸, a power law of a photon index of 2.1 absorbed with a hydrogen column density of $N_{\text{H}} = 2.6 \times 10^{21} \text{ cm}^{-2}$, and no flux variability are assumed for simplicity. We confirm that the choice of the spectrum for the PSF model does not affect the determination of the flux by the image fitting because the energy dependence of the PSF is not very large in the energy band of interest. To suppress the statistical fluctuation in the PSF model, we generate a sufficiently large number of photons for each source candidate by assuming a flux of 50 mCrab. The simulated events of the PSF data are processed in the same way as for the real data, and are converted into images in the sky coordinates.

(5) DETERMINING FLUXES AND POSITIONS WITH IMAGE FIT

To determine the fluxes and positions of the source candidates, we perform image fitting to the real data with a model consisting of the background and PSF models, both produced by the simulations as described above. Here the fits to all of the source candidates and the background are performed simultaneously in each image. The best-fit parameters are determined with the Poisson likelihood algorithm where the

¹⁸ The spectral parameters are adopted from the INTEGRAL General Reference Catalog (ver. 35). <http://www.isdc.unige.ch/integral/science/catalogue>

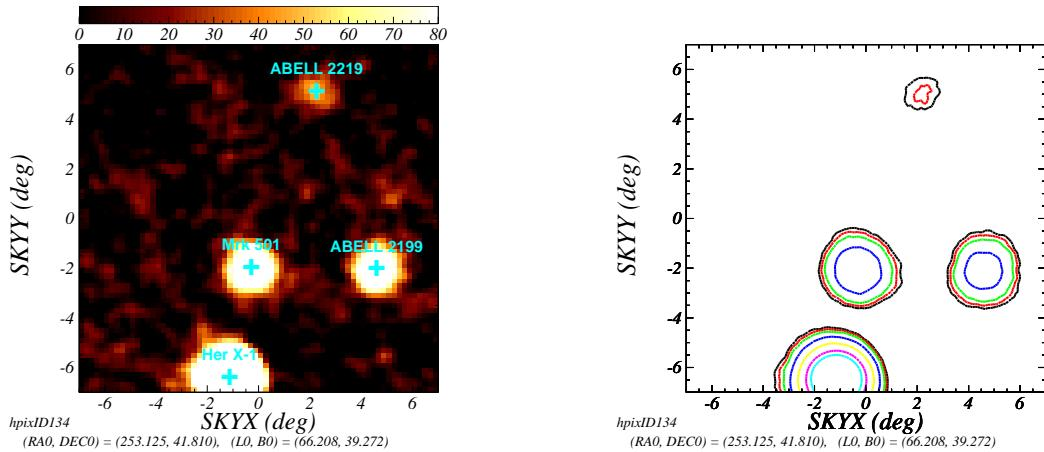


FIG. 4.— (Left) Example of a smoothed image of the real data. The image size is $14^\circ \times 14^\circ$, whose center is located at $(\text{R.A.}, \text{Decl.}) = (253.125^\circ, 41.810^\circ)$. The best-fit background model obtained from image fitting is subtracted. The four cyan crosses represent the locations of detected sources with $s_{D,4-10\text{keV}} \geq 7$. (Right) Significance map of the same region. The contours display the significance levels of 5 (black), 7 (red), 10 (green), 20 (blue), 40 (yellow), 70(magenta), and 90(cyan), from outer to inner.

so-called C statistics (Cash 1979) is minimized, defined as

$$C \equiv 2 \sum_{i,j} \{M(i,j) - D(i,j) \ln M(i,j)\}, \quad (1)$$

where $D(i,j)$ and $M(i,j)$ represent the data and model at the image pixel (i,j) , respectively. The parameter that gives a C value larger by unity than that of the best-fit with the other free parameters allowed to float corresponds to its 1σ error. The MINUIT package is utilized in the minimization. In the fitting, we change the bin width of an image from 0.1° to 0.2° for the fit to converge faster, and only treat the inner $11^\circ \times 11^\circ$ region of the image for the calculation to ignore the influence by sources located just outside the whole image with a size of $14^\circ \times 14^\circ$. For the PSF models of source candidates located in the inner $11^\circ \times 11^\circ$ region of the image, their normalizations and positions are set to be free, as well as the overall background level. The PSF normalization of each source gives its flux corrected for exposure and the instrumental response in units of “Crab” because we basically measure its total counts relative to that would be observed from the Crab Nebula on which the PSF simulation is based. Since it is difficult to accurately determine the position of a source outside the $11^\circ \times 11^\circ$ region whose PSF is distributed beyond the image boundary, we fix it at the location originally detected in the significance map. It is found that in a few images containing very bright sources such as Sco X-1 and Cyg X-2, the background level cannot be properly determined due to the incomplete reproduction of the PSF shape. In such cases, we fix the background level to the value obtained in the second step.

After the fitting, we calculate the detection significance in the 4–10 keV ($s_{D,4-10\text{keV}}$) for each source candidate, defined as

$$s_{D,4-10\text{keV}} \equiv (\text{best-fit 4-10 keV flux}) / (\text{its } 1\sigma \text{ statistical error}). \quad (2)$$

Here we use the MINOS negative error in the MINUIT package as the flux error, although the positive and negative errors are consistent with each other in almost all cases because the number of source counts is always sufficiently high that symmetric errors are a reasonable approximation. We adopt $s_{D,4-10\text{keV}} \geq 7$ for the criterion of source detection, considering the number of fake sources caused by the fluctuation of background level (see section 4.2).

(6) ITERATION OF SOURCE SEARCH AND IMAGE FIT

Due to source confusion, multiple close sources can be detected as a single object. To salvage such sources located in a source crowded region as much as possible, we again perform the source search in the second step but by adopting the best-fit total model consisting of PSFs and the background obtained in the previous step as a new background. Here we adopt a more conservative detection criterion of 5.5σ than in the first round to reduce the probability of fake detections around the existing sources. This procedure gives us an additional source-candidate list containing 135 objects above 5.5σ at $|b| > 10^\circ$. The first and second source-candidate lists are merged into one list. We then repeat the image fitting using the revised source-candidate list, and obtain the final list of sources detected with $s_{D,4-10\text{keV}} \geq 7$ in the 4–10 keV band.

(7) MEASUREMENT OF 3–4 KEV FLUX

To obtain spectral information, we also determine the 3–4 keV fluxes of all sources in the final list created above. The images of real data, background model, and PSF models in the 3–4 keV band are produced in the same way as for those in the 4–10 keV band. We then perform image fitting to the 3–4 keV band image using the source-candidate list obtained in the 6th step. The source positions are fixed at those determined by the image fit in the 4–10 keV band. Thus, we finally derive the 3–4 keV fluxes and their errors for all the sources detected in the 4–10 keV band. Using the 4–10 keV and 3–4 keV fluxes, which are independently determined from the images of the two energy bands, we calculate the hardness ratio (HR) defined as

$$\text{HR} = \frac{H - S}{H + S}, \quad (3)$$

where H and S represent the observed fluxes in the 4–10 keV and 3–4 keV bands, respectively. The error of the HR is calculated by simple propagation of those in H and S , both can be regarded as symmetric errors.

4. CATALOG

4.1. Basic Properties

In this section, we present the second MAXI/GSC X-ray source catalog in the high Galactic latitude sky obtained from the 37-month all-sky survey data in the 4–10 keV band.

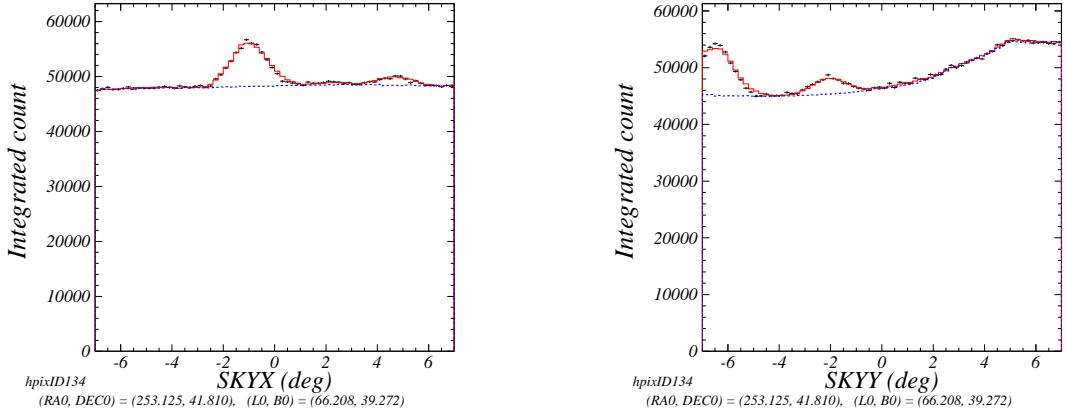


FIG. 5.—Projected images onto the X -axis (left) and Y -axis (right) of the same region as shown in figure 4. The black points represent the real data with 1σ Poisson errors. The two color lines display the best-fit models (red-solid: total, blue-dashed: only background).

It consists of 500 sources detected with a significance of $s_{D,4-10\text{keV}} \geq 7$ at $|b| > 10^\circ$. Table 1 gives the catalog with columns of (1) source identification number, (2) MAXI source name based on the best-fit position in the final image fit (with a prefix of “2MAXI”), (3)-(4) best-fit position in the equatorial coordinates in units of degree, (5) σ_{stat} : 1σ statistical position error in units of degree (the squared sum of those in the X - and Y -directions), (6) $s_{D,4-10\text{keV}}$: 4–10 keV detection significance, (7) $f_{4-10\text{keV}}$: observed 4–10 keV flux and its 1σ error in units of $10^{-12} \text{ ergs cm}^{-2} \text{ s}^{-1}$, (8) $s_{D,3-4\text{keV}}$: 3–4 keV detection significance, (9) $f_{3-4\text{keV}}$: observed 3–4 keV flux and its 1σ error in units of $10^{-12} \text{ ergs cm}^{-2} \text{ s}^{-1}$, (10) HR: hardness ratio and its 1σ error, (11) counterpart name, (12)–(13) position of the counterpart (14) redshift, (15) type, (16) cross-matching flag, and (17) note.

Taking into account the MAXI/GSC response, we calculate the dependences of the hardness ratio HR on spectral parameters and those of the conversion factors from an area-corrected count rate (defined as that relative to the Crab one) into an energy flux in the same energy band, C_{4-10} and C_{3-4} . In the top-left panel of figure 6, the hardness ratio is plotted as a function of photon index with an unabsorbed power-law spectrum, whereas in the top-right panel it is given as a function of column density of an absorbed power-law spectrum with a photon index of 1.8 at redshift of 0. In the middle and bottom panels, we also display the dependences of the conversion factors on the same spectral parameters in the 4–10 keV and 3–4 keV bands, respectively. The expected values of HR and conversion factors are $\text{HR}=0.0745$, $C_{4-10}=1.24 [10^{-11} \text{ ergs cm}^{-2} \text{ s}^{-1}] / [\text{mCrab}]$, $C_{3-4}=0.401 [10^{-11} \text{ ergs cm}^{-2} \text{ s}^{-1}] / [\text{mCrab}]$ for a photon index of 1.8 with no absorption, and $\text{HR}=0.000$, $C_{4-10}=1.21 [10^{-11} \text{ ergs cm}^{-2} \text{ s}^{-1}] / [\text{mCrab}]$, $C_{3-4}=0.398 [10^{-11} \text{ ergs cm}^{-2} \text{ s}^{-1}] / [\text{mCrab}]$ for the Crab Nebula-like spectrum (see section 3.2 for its spectral parameters). The energy fluxes listed in the catalog are all calculated by assuming the Crab Nebula-like spectrum.

The correlation between the flux and the detection significance in the 4–10 keV band are plotted in figure 7. The detection significance, s_D , can be approximated as $St/\sqrt{St+Bt}$, where S and B are the count rates of the source and background, respectively, and t is exposure. Thus, in the high flux range ($s_D \sim \sqrt{St}$), the detection significance is expected to be proportional to $(\text{flux})^{1/2}$. In contrast, it is proportional to $(\text{flux})^1$ in the low flux range ($s_D \sim S\sqrt{t/B}$). These trends

are confirmed in the figure. The limiting sensitivity with $s_{D,4-10\text{keV}} \geq 7$ (that of the faintest source detected) corresponds to $\sim 5 \times 10^{-12} \text{ ergs cm}^{-2} \text{ s}^{-1}$ ($\sim 0.4 \text{ mCrab}$) in the 4–10 keV band.

4.2. Number of Spurious Sources

Since we conservatively adopt the detection threshold of $s_D \geq 7$, fake detections by statistical fluctuation in photon counts are expected to be negligible. However, the catalog may contain a small fraction of spurious sources caused by remaining systematic errors in the background model. To simply estimate the number of such sources, we search for “negative” signals from the smoothed net-source maps produced in the second step of section 3.2. This gives a “negative” source-candidate list consisting of 50 objects below -7σ from the entire sky. Performing image fitting by adding negative PSFs to the model, we find that the number of final “negative” detections with $s_D \leq -7$ becomes only 18% of that of spurious source candidates. The reduction is expected because the shape of residual signals due to improper modeling of the background profile is very different from that of the PSF. Thus, we estimate that our catalog would include ~ 9 spurious detections, which are less than 2% of the total sources. Note that if we instead adopt $s_D \geq 6$ as the detection criterion for the catalog, we find that the fraction of spurious ones becomes $\sim 5\%$ of the total, which is too high to be accepted.

4.3. Cross Matching with Other X-ray Catalogs

Identification of X-ray sources with counterparts in other wavelengths is very important for further scientific studies using an X-ray catalog. The most critical information for this task is the position accuracy. Figure 8 plots the correlation between the flux and position error of the MAXI sources. As noticed, σ_{stat} is roughly proportional to $(s_{D,4-10\text{keV}})^{-1}$, as expected from a simple statistical argument on the accuracy of the centroid determination of the PSF with limited photon counts. A typical 1σ error becomes $\sigma_{\text{stat}} \sim 0.2^\circ$ at $s_{D,4-10\text{keV}} = 7$.

Considering the large positional uncertainties of MAXI, it is difficult to directly match them with those in optical/infrared catalogs with large number densities. However, since the MAXI sources represent brightest X-ray populations, a significant fraction of them are expected to be included by other X-ray catalogs at similar flux levels covering

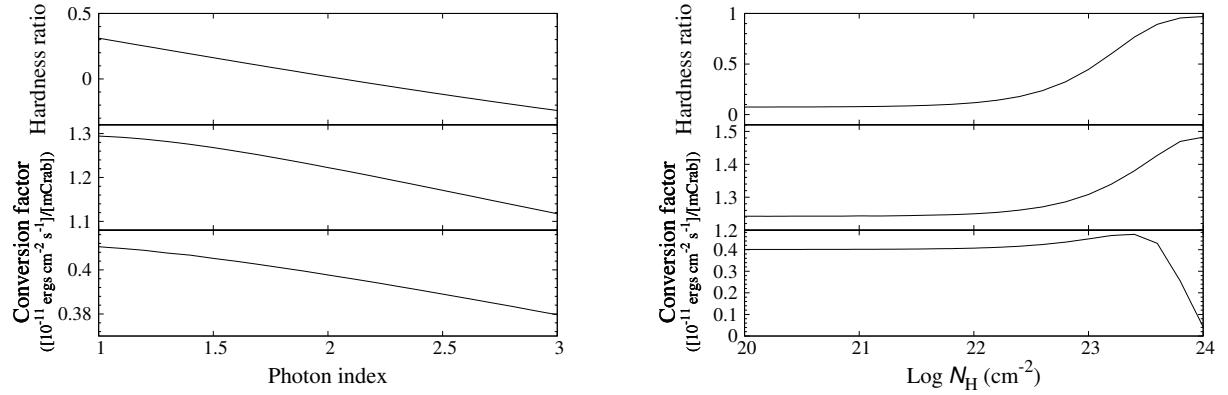


FIG. 6.— (Top) Hardness ratio between the 4–10 keV and 3–4 keV bands (HR) given as a function of a spectral parameter. (Middle) The conversion factor from a count rate (defined as that relative to the Crab one) to an energy flux in the 4–10 keV band for different spectral parameters in units of [$10^{-11} \text{ ergs cm}^{-2} \text{s}^{-1}/[\text{mCrab}]$]. (Bottom) The same as above but in the 3–4 keV band. (Left) The parameter is the photon index of a power law with no absorption. (Right) The parameter is the absorption column density for a power law with a photon index of 1.8.

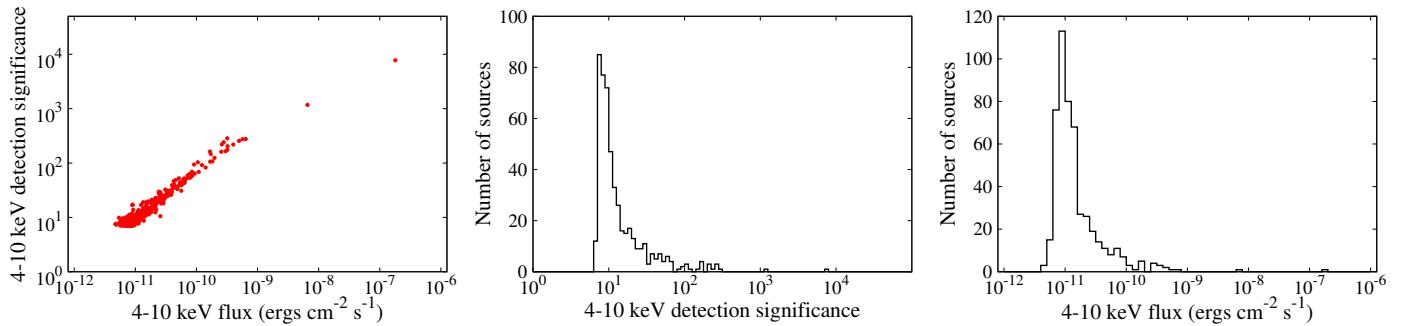


FIG. 7.— Correlation between the flux and the detection significance in the 4–10 keV band (left), histogram of the 4–10 keV flux (middle), and that of 4–10 keV detection significance (right) for all the sources in the catalog.

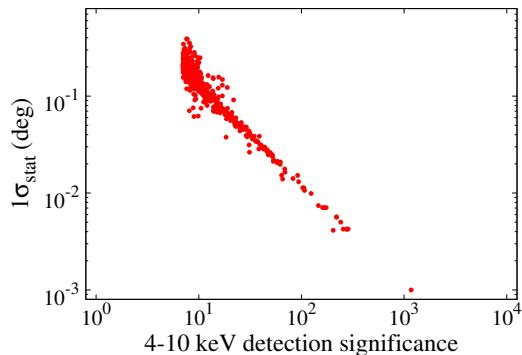


FIG. 8.— Correlation between the 4–10 keV detection significance ($s_{\text{d},4-10\text{keV}}$) and the 1σ positional error (σ_{stat}).

a wide sky area. Hence, as the first step of identification work, we cross-match our sources with two major X-ray catalogs to determine the most likely counterparts: the Swift/BAT hard X-ray (14–195 keV) all-sky survey 70-month catalog (hereafter, BAT70; Baumgartner et al. 2012) and the Meta-Catalog of X-Ray Detected Clusters of Galaxies (hereafter, MCXC; Piffaretti et al. 2011). The latter is based on the ROSAT all-sky survey and ROSAT serendipitous surveys performed in the energy bands below ~ 2 keV. While BAT70 provides an X-ray sample including heavily obscured objects, MCXC complements the identification of galaxy clusters, which are hard to be detected above 10 keV due to their soft spectra.

The cross-matching of the MAXI sources with these catalogs is carried out in the following way. We firstly search for

counterparts from the BAT70 catalog. Then, for those without BAT counterparts, we use the MCXC. Finally, we also perform cross-matching with the first MAXI/GSC source catalog (hereafter, GSC7; Hiroi et al. 2011). Basically, we refer to the positions of the optical/infrared counterparts in these catalogs instead of the X-ray positions, except for a few sources in the first MAXI/GSC catalog that do not have unique optical counterparts. As the position errors of the MAXI sources, we consider both statistical error (σ_{stat}) and systematic error (σ_{sys}) related to the instrument calibration and attitude determination of MAXI. Since the two errors are independent of each other, we define the total 1σ position error (σ_{posi}) as the root sum squares:

$$\sigma_{\text{posi}} \equiv \sqrt{\sigma_{\text{stat}}^2 + \sigma_{\text{sys}}^2}. \quad (4)$$

In the matching process, we set the 1σ systematic error as $\sigma_{\text{sys}} = 0.05^\circ$ on the basis of the previous work (Hiroi et al. 2011), and use an error circle with a radius of $r = 2.5\sigma_{\text{posi}}$, which corresponds to 95% confidence level in the 2-dimensional space giving a typical increment in the C value by 6.0. The position errors in the reference catalogs are ignored, since they are much smaller than those of the MAXI sources.

The cross-matching results are listed in columns (11)–(15) of table 1 for each source. The locations of the MAXI sources in the Galactic coordinates are plotted in figure 9. The numbers of matched MAXI sources in a single or two reference

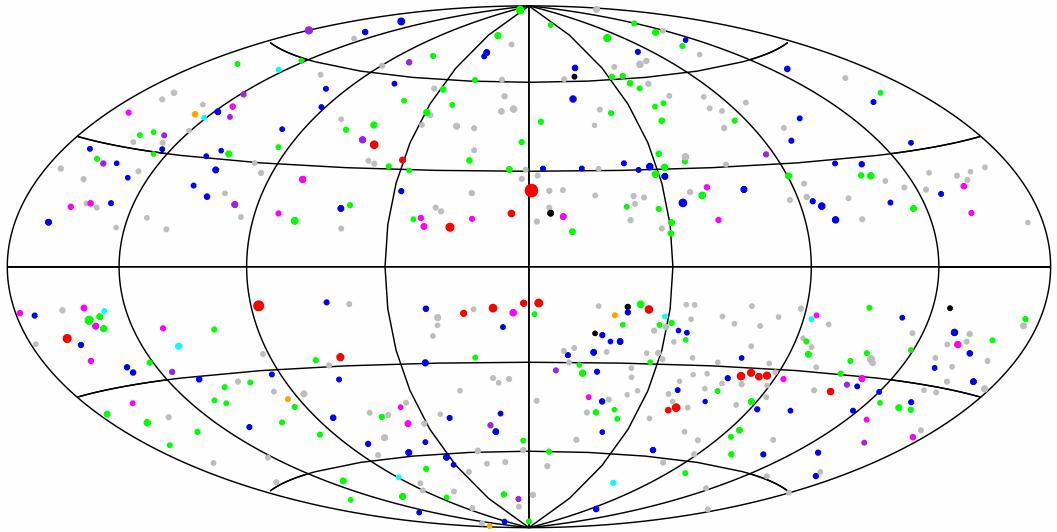


FIG. 9.— Locations of all the MAXI sources in the Galactic coordinates. The center is at $(l, b) = (0^\circ, 0^\circ)$. The radii of the circles are proportional to the logarithm of the fluxes. Different colors correspond to different types: unidentified X-ray sources in BAT70 (black); galaxies (cyan); galaxy clusters (green); Seyfert galaxies, blazars (purple); CVs/Stars (magenta); X-ray binaries (red); confused sources (orange); sources without counterparts in BAT70 or MCXC (gray).

TABLE 2
NUMBER OF MATCHED MAXI SOURCES.

Catalog name	BAT70	MCXC	GSC7	One catalog only ^a
BAT70	185 (187) ^b	23	84	92
MCXC	123 (130) ^b	37	78
GSC7	114 (114) ^b	8

NOTE.— Numbers of MAXI sources matched with both catalogs are listed.

^aNumbers of MAXI sources matched only with one catalog given in the first column.

^bNumbers in parentheses represent those of total matched counterparts in each catalog.

TABLE 3
CATEGORIES OF CATALOGED SOURCES.

Category	Number of sources
unidentified	5
galaxies	8
galaxy clusters	114
Seyfert galaxies	100
blazars	15
CVs/Stars	30
X-ray binaries	20
confused	4
unmatched	204

catalogs in any combination from the three reference catalogs are summarized in table 2. We also show the total numbers of counterparts in each reference catalog with parentheses; here we count more than one objects in the same reference catalog if they are located within the error radius of the MAXI source. In such cases, we adopt the one with the smallest angular separation from the MAXI position as the most likely counterpart used for the definition of source type. As a result, we find that 296 out of the 500 sources in the present catalog have one or more counterparts. The numbers of each source type are as shown in table 3: 2 unidentified X-ray sources in BAT70, 8 galaxies, 114 galaxy clusters, 100 Seyfert galaxies, 15 blazars, 30 CVs/Stars, 20 X-ray (neutron/black-hole) binaries, 4 confused objects, and 204 sources without counterparts in BAT70 or MCXC.

In the above procedure, some of the MAXI sources may be matched to those in the BAT70 catalog and MCXC by chance. Here we estimate the number of such coincidental match, N_{CM} , calculated as

$$N_{CM} = \rho_{BAT70} \times S_{BAT70} + \rho_{MCXC} \times S_{MCXC}, \quad (5)$$

where $\rho_{BAT70(MCXC)}$ and $S_{BAT70(MCXC)}$ represent the source number densities of BAT70 (MCXC) at $|b| > 10^\circ$ and the total areas of the error circles of the MAXI sources used for the cross-matching with those catalogs. Specifically, we use the following values: $\rho_{BAT70} = 0.025 (\text{deg}^{-2})$, $\rho_{MCXC} = 0.050 (\text{deg}^{-2})$, $S_{BAT70} = 236.8 (\text{deg}^2)$, and $S_{MCXC} = 173.9 (\text{deg}^2)$. We thus estimate $N_{CM} = 10.3$, which is $\sim 3\%$ of the total number of the matched sources.

4.4. Position Accuracy

We here examine the actual positional error of MAXI as a function of detection significance in the 4–10 keV band on the basis of the cross matching result. We calculate the angular separation between the MAXI position and that of the most likely counterpart for each object. Figure 10 shows the histograms of the angular separation for all the matched sources in different significance bins (left: $s_{D,4-10\text{keV}} = 7 - 12$, middle: $s_{D,4-10\text{keV}} = 12 - 80$, and right: $s_{D,4-10\text{keV}} > 80$). Figure 11 plots 90% error radii as a function of 4–10 keV detection significance that are directly obtained from the observed histograms. The black crosses represent those in the bins of $s_{D,4-10\text{keV}} = 7-9, 9-12, 12-25, 25-80$, and > 80 , from left to right. We fit these data with the form of

$$\sigma_{\text{posi}}^{90\%} = \sqrt{(A/s_{D,4-10\text{keV}})^B + C^2}, \quad (6)$$

where A , B , and C are free parameters. The blue curve in figure 11 represents the best-fit with $A = 2.93 \pm 0.47$, $B = 1.80 \pm 0.22$, and $C = 0.09 \pm 0.01$. The slope B is close to 2.0 as expected from the theory. From this result, we estimate the 90% systematic error to be $\approx 0.09^\circ$, which is consistent with that derived in the previous study (Hiroi et al. 2011).

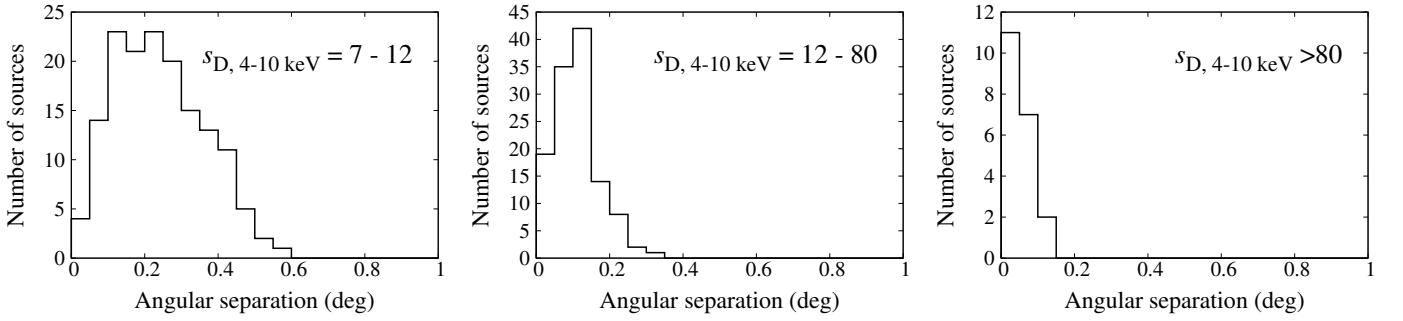


FIG. 10.— Histograms of the angular separation between the positions of the MAXI sources and those of their most-likely counterparts in the reference catalogs. The left, center, and right panel include the objects with the significance level of $s_{D,4-10\text{keV}}$ = 7–12, 12–80, and >80, respectively.

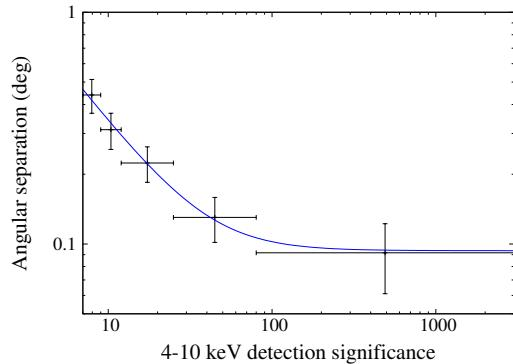


FIG. 11.— 90% error radius of MAXI sources as a function of detection significance in the 4–10 keV band. The black points denote the data and the blue curve represents the best-fit model with the form of $\sqrt{(A/s_{D,4-10\text{keV}})^B + C^2}$, where $A = 2.9 \pm 0.5$, $B = 1.8 \pm 0.2$, and $C = 0.09 \pm 0.01$.

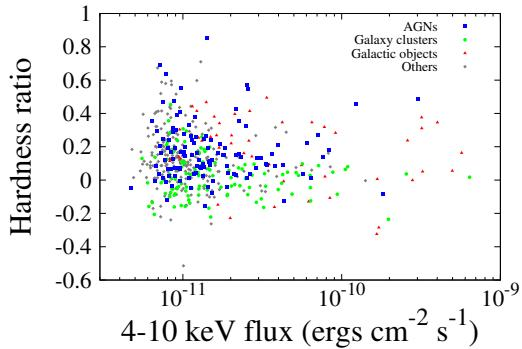


FIG. 12.— Flux in the 4–10 keV band versus HR plot for the catalogued sources with different types: AGNs (blue squares), galaxy clusters (green circles), Galactic/LMC/SMC objects (red triangles), and others (i.e., sources without unique identification; gray diamonds). The typical errors of the HR at $f_{4-10\text{keV}}$ of 10^{-10} and 10^{-11} ergs cm⁻² s⁻¹ are ~ 0.01 and ~ 0.09 , respectively. For visibility, two points with the largest fluxes of $f_{4-10\text{keV}} > 10^{-9}$ cm⁻² s⁻¹, corresponding to Sco X-1 and Cyg X-2, are excluded from this figure.

4.5. Hardness Ratio Distribution

Figure 12 plots the diagram between the 4–10 keV flux and hardness ratio (HR) for the catalogued sources with different types. The blue squares and green circles represent AGNs and galaxy clusters, respectively. The red triangles correspond to Galactic objects and large/small Magellanic cloud (LMC/SMC) objects. Sources without unique identification (i.e., those with no counterpart or multiple ones) are denoted as the gray diamonds. Figure 13 displays the histograms of HR for each

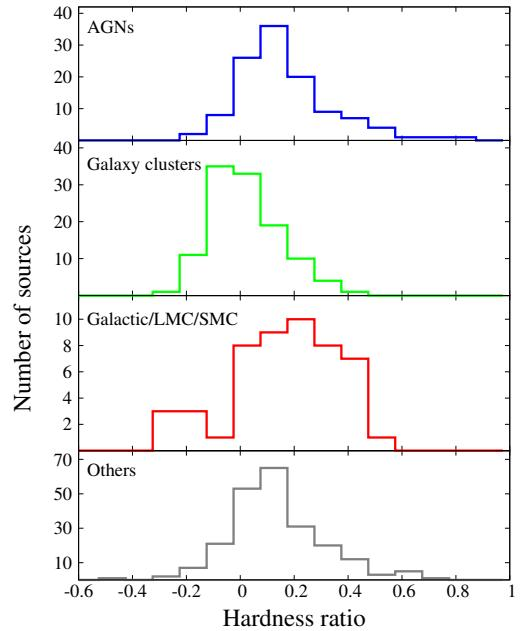


FIG. 13.— Histograms of HR shown in figure 12 for each type: from top to bottom, AGNs, galaxy clusters, Galactic/LMC/SMC, and others.

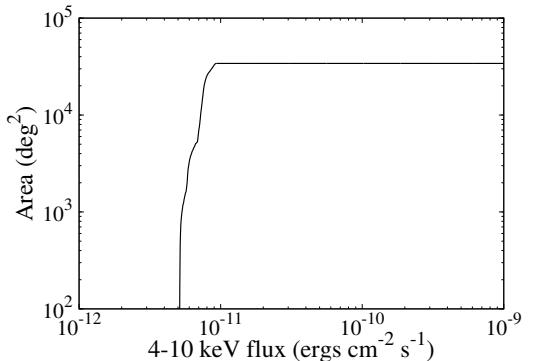


FIG. 14.— Area curve with detection significance of $s_{D,4-10\text{keV}} > 7$ plotted against 4–10 keV flux for the MAXI/GSC 37-month survey at $|b| > 10^\circ$.

type. The HR distribution of galaxy clusters is located at lower values than that of AGNs. This is consistent with the expectation that galaxy clusters have softer spectra than AGNs in the 3–10 keV range.

4.6. Log N-log S Relation

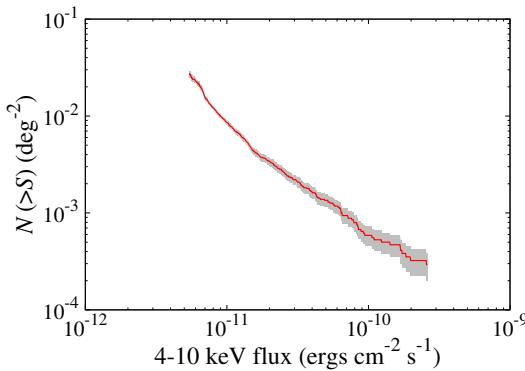


FIG. 15.— Log N -log S relation in the 4–10 keV band derived from the MAXI/GSC 37-month survey at $|b| > 10^\circ$. All the 500 sources are included in the calculation. The gray-shaded area represents the 1σ statistical error region calculated from the source counts.

We derive the source number counts (log N -log S relation) in the 4–10 keV band based on the MAXI/GSC 37-month catalog. For this calculation, we need the so-called area curve, which represents a survey area guaranteed for detection of a source given as a function of flux. In the same way as in Hiroi et al. (2011), we estimate the sensitivity at each sky position on the basis of the background photon counts and “effective” exposure (i.e., exposure \times detector area). Figure 14 displays the area curve in the 4–10 keV band for the detection significance of $s_{D,4-10\text{keV}} > 7$. As noticed from the figure, the sensitivity at the deepest exposure reaches to ~ 0.4 mCrab ($\sim 5 \times 10^{-12}$ ergs $\text{cm}^{-2} \text{s}^{-1}$ in the 4–10 keV band), which is consistent with the faintest flux level of the cataloged sources.

Dividing the flux distribution of the detected sources by the survey area, we obtain the log N -log S relation in the differential form. Figure 15 shows the log N -log S relation of all the MAXI sources in the integral form, where the total number density $N(>S)$ for sources with fluxes above S is plotted. The results at fluxes above 1.5×10^{-11} ergs $\text{cm}^{-2} \text{s}^{-1}$ perfectly match with those of Hiroi et al. (2011) derived from the 7-month data. In the faintest range below 7×10^{-12} ergs cm^{-2}

s^{-1} , however, the number density is slightly (by $\sim 10\%$) larger than that extrapolated from the brighter flux range. This is most probably attributable to the effects by source confusion, which is unavoidable at faintest fluxes close to a confusion limit determined by the PSF size. The effects may have to be taken into account in future studies using this catalog, depending on the scientific goals.

5. CONCLUSION

We present the second MAXI/GSC source catalog in the high Galactic-latitude sky based on the 37-month data in the 4–10 keV band observed from 2009 September to 2012 October. The accuracy of the background model is significantly improved from our previous work (Hiroi et al. 2011) by considering the dependence of the background rate on the “VC” monitor count sensitive to high energy particles. Through the image fitting to tangentially-projected images with the Poisson likelihood algorithm, we finally detect 500 X-ray sources at $|b| > 10^\circ$ with the detection significance $s_{D,4-10\text{keV}} \geq 7$. The limiting sensitivity is ~ 0.6 mCrab, or 7.5×10^{-12} ergs $\text{cm}^{-2} \text{s}^{-1}$ (4–10 keV) for 50% of the survey area, which is the highest ever achieved among all-sky missions covering this energy band. Performing cross-matching with other X-ray source catalogs, we find that 296 sources have one or more than one counterparts. The identification work of a complete sample from this catalog is on-going, which will be reported in future papers.

This work makes use of the HEALPix (Górski et al. 2005) package. This work was partly supported by the Grant-in-Aid for JSPS Fellows for young researchers (KH), Scientific Research 23540265 (YU), and by the grant-in-aid for the Global COE Program “The Next Generation of Physics, Spun from Universality and Emergence” from the Ministry of Education, Culture, Sports, Science and Technology (MEXT) of Japan.

REFERENCES

- Baumgartner, W. H., et al. 2010, ApJS, submitted
- Baumgartner, W. H., Tueller, J., Markwardt, C. B., et al. 2012, arXiv:1212.3336
- Beckmann, V., Gehrels, N., Shrader, C. R., & Soldi, S. 2006, ApJ, 638, 642
- Beckmann, V., Soldi, S., Ricci, C., et al. 2009, A&A, 505, 417
- Bird, A. J., Malizia, A., Bazzano, A., et al. 2007, ApJS, 170, 175
- Bird, A. J., Bazzano, A., Bassani, L., et al. 2010, ApJS, 186, 1
- Cash, W. 1979, ApJ, 228, 939
- Cusumano, G., La Parola, V., Segreto, A., et al. 2010, A&A, 524, A64
- Eguchi, S., Hiroi, K., Ueda, Y., et al. 2009, Astrophysics with All-Sky X-Ray Observations, 44
- Górski, K. M., Hivon, E., Banday, A. J., et al. 2005, ApJ, 622, 759
- Hayashida, K., Inoue, H., Koyama, K., Awaki, H., Takano, S., 1989, PASJ, 41, 373
- Hiroi, K., Ueda, Y., Isobe, N., et al. 2011, PASJ, 63, 677
- Kravonos, R., Revnivtsev, M., Lutovinov, A., Sazonov, S., Churazov, E., & Sunyaev, R. 2007, A&A, 475, 775
- Matsuoka, M., Kawasaki, K., Ueno, S., et al. 2009, PASJ, 61, 999
- Mihara, T., Nakajima, M., Sugizaki, M., et al. 2011, PASJ, 63, 623
- Piffaretti, R., Arnaud, M., Pratt, G. W., Pointecouteau, E., & Melin, J.-B. 2011, A&A, 534, A109
- Sugizaki, M., Mihara, T., Serino, M., et al. 2011, PASJ, 63, 635
- Tawa, N., Hayashida, K., Nagai, M., et al. 2008, PASJ, 60, 11
- Tueller, J., Mushotzky, R. F., Barthelmy, S., et al. 2008, ApJ, 681, 113
- Tueller, J., Baumgartner, W. H., Markwardt, C. B., et al. 2010, ApJS, 186, 378
- Ueda, Y., Hiroi, K., Isobe, N., et al. 2011, PASJ, 63, 937
- Voges, W., Aschenbach, B., Boller, T., et al. 1999, A&A, 349, 389
- Voges, W., Aschenbach, B., Boller, T., et al. 2000, IAU Circ., 7432, 3

TABLE I
PROPERTIES OF SOURCES IN THE SECOND MAXI/GSC CATALOG.

(2)	MAXI	(3)	(4)	(5)	(6)	(7)	(8)	(9)	(10)	(11)	(12)	(13)	(14)	(15)	(16)	(17)
	Name	R.A.	Decl.	$\sigma_{\text{stat}}^{[a]}$	$\sigma_{\text{syst}}^{[a]}$	$f_{\text{D},4-10\text{keV}}^{[b]}$	$f_{\text{D},4-10\text{keV}}^{[b]}$	$f_{\text{3-4keV}}^{[c]}$	HR	Name ^[d]	R.A.	Decl.	z	Type ^[e]	Flag ^[f]	Note ^[g]
1	2MAXI J0000-774	0.0	-77.4	0.170	10.4	8.0±0.8	7.6	1.9±0.3	0.15±0.08	RXC J0005.3+1612	1.344	16.211	0.1164	Galaxy Cluster	M	
2	2MAXI J0004+160	1.1	16.0	0.141	7.5	10.0±1.3	4.6	1.7±0.4	0.31±0.12							
3	2MAXI J0004+726	1.2	72.7	0.118	11.1	10.0±0.9	12.3	3.6±0.3	-0.05±0.06							
4	2MAXI J0008-691	2.1	-69.2	0.120	9.2	6.7±0.7	5.8	1.5±0.3	0.20±0.10							
5	2MAXI J0009-817	2.5	-81.8	0.250	9.8	5.4±0.5	6.1	1.6±0.3	0.05±0.10							
6	2MAXI J0011-112	2.8	-11.2	0.122	9.0	9.7±1.1	6.5	2.2±0.3	0.18±0.09							
7	2MAXI J0012-152	3.1	-15.2	0.184	7.6	7.5±1.0	7.5	2.5±0.3	0.00±0.09	MACS10011.7-1523	2.928	-15.389	0.378	Galaxy Cluster	M	
8	2MAXI J0012-294	3.1	-29.5	0.148	17.0	9.1±0.5	10.0	3.5±0.4	-0.09±0.06							
9	2MAXI J0021+286	5.4	28.7	0.132	8.3	11.1±1.3	9.1	3.4±0.4	0.03±0.08	RXC J0020.6+2840	5.170	28.675	0.094	Galaxy Cluster	M	
10	2MAXI J0023-193	5.8	-19.3	0.130	10.1	10.8±1.1	9.4	3.1±0.3	0.06±0.07							
11	2MAXI J0037-790	9.3	-79.1	0.130	17.0	8.9±0.5	9.9	2.5±0.3	0.07±0.06	2MASX J00341665-7905204	8.570	-79.089	0.074	Sy1	B	
12	2MAXI J0041-285	10.3	-28.6	0.119	7.6	8.2±1.1	4.4	1.5±0.3	0.28±0.12	RXC J0042.1-2832	10.536	-28.536	0.1082	Galaxy Cluster	M	
13	2MAXI J0041-092	10.4	-9.2	0.030	43.9	53.3±1.2	41.5	16.5±0.4	0.03±0.04	MACS10041.0-092	10.408	-9.342	0.0551	Galaxy Cluster	BMG	
14	2MAXI J0043+412	10.8	41.3	0.045	26.6	38.8±1.5	27.8	12.2±0.4	0.02±0.03	M31 (2)	10.668	41.200	0.083	Galaxy Cluster	BG	
15	2MAXI J0043+247	10.9	24.7	0.205	7.5	8.3±1.1	8.8	3.2±0.4	-0.07±0.09	ZwCl235	10.967	24.402	0.083	Sy1	B	
16	2MAXI J0044-238	11.0	-23.8	0.209	7.3	7.8±1.1	1.7	0.6±0.3	0.64±0.18	NGC 235A	10.720	-23.541	0.0222	Galaxy Cluster	B	
17	2MAXI J0047-754	11.8	-75.4	0.159	8.5	6.6±0.8	8.4	2.1±0.3	0.01±0.08							
18	2MAXI J0048+320	12.2	32.0	0.077	16.0	21.4±1.3	7.3	2.8±0.4	0.42±0.06	Mrk 348 (3)	12.196	31.957	0.015	Sy2/FSRQ	BG	
19	2MAXI J0051-725	12.8	-72.6	0.038	29.6	24.1±0.8	21.1	5.7±0.3	0.16±0.03	2E0050.1-7247 (4)	12.972	-72.530		HMXB	G	
20	2MAXI J0052+176	13.0	17.6	0.136	10.1	12.2±1.2	7.7	2.9±0.4	0.16±0.08	Mrk 1148	12.978	17.433	0.064	Sy1	B	
21	2MAXI J0055+463	13.9	46.3	0.120	9.8	13.1±1.3	7.0	2.7±0.4	0.24±0.08	1RXS J005528.0+461143 (5)	13.833	46.216		CV/DQ Her	BG	
22	2MAXI J0055+259	14.0	26.0	0.173	7.9	9.4±1.2	9.1	3.3±0.4	-0.04±0.08	A115	13.999	26.378	0.1971	Galaxy Cluster	M	
23	2MAXI J0056-011	14.1	-1.2	0.060	21.5	26.1±1.2	23.8	9.4±0.4	-0.04±0.03	RXC J0056.3-0112 (6)	14.076	-1.217	0.0442	Galaxy Cluster	MG	
24	2MAXI J0102-222	15.5	-22.3	0.140	9.5	10.5±1.1	13.6	4.7±0.3	-0.15±0.06							
25	2MAXI J0105-241	16.4	-24.2	0.216	7.6	7.6±1.0	7.0	2.5±0.4	0.01±0.10	RXC J0104.5-2400 (C)	16.146	-24.000	0.1603	Galaxy Cluster	M	
26	2MAXI J0107-468	16.8	-46.8	0.248	10.3	12.0±1.2	5.2	2.0±0.4	0.32±0.10	ESO 243-G 026	16.408	-47.072	0.0193	Sy1	BM	
27	2MAXI J0111-148	18.0	-14.9	0.388	7.7	7.9±1.0	9.8	3.3±0.3	-0.12±0.08	Mrk 1152	18.459	-14.846	0.0527	HMXB/NS	BG	
28	2MAXI J0117-734	19.3	-73.4	0.004	285.0	318.5±1.1	139.3	54.9±0.4	0.31±0.00	SMC X-1 (7)	19.271	-73.443		BL Lac	BG	
29	2MAXI J0123+342	20.8	34.3	0.127	11.3	15.2±1.3	14.5	5.8±0.4	-0.08±0.06	SHBL J012308.7+342049 (8)	20.786	34.347	0.272	Sy1	B	
30	2MAXI J0124-588	21.0	-58.8	0.065	18.6	17.9±1.0	15.0	4.3±0.3	0.15±0.04	Fairall 9	20.941	-58.806	0.047	Sy1	B	
31	2MAXI J0124-349	21.0	-35.0	0.069	18.6	22.5±1.2	14.3	5.4±0.4	0.16±0.04	NGC 526A	20.977	-35.065	0.0191	Sy1	B	
32	2MAXI J0126+081	21.5	8.2	0.177	8.4	10.3±1.2	9.3	3.5±0.4	-0.02±0.08							
33	2MAXI J0134-082	23.6	-8.2	0.174	7.1	7.9±1.1	5.9	2.0±0.3	0.12±0.11	RXC J0132.6-0804	23.170	-8.072	0.1489	Galaxy Cluster	M	
34	2MAXI J0151+361	28.0	36.1	0.087	11.2	14.9±1.3	17.5	7.7±0.4	-0.22±0.05	RXC J0152.7+3609	28.195	36.151	0.0163	Galaxy Cluster	M	
35	2MAXI J0157-838	29.3	-83.9	0.188	7.7	5.9±0.8	5.9	1.6±0.3	0.09±0.11							
36	2MAXI J0157-528	29.4	-52.8	0.091	9.2	11.1±1.2	9.5	3.0±0.3	0.09±0.08							
37	2MAXI J0202-727	30.7	-72.8	0.128	10.9	8.3±0.8	4.4	1.1±0.2	0.43±0.10							
38	2MAXI J0205-020	31.4	-2.1	0.147	9.6	11.3±1.2	7.5	2.7±0.4	0.16±0.08							
39	2MAXI J0206-166	31.6	-16.6	0.179	8.7	9.2±1.1	6.7	2.2±0.3	0.16±0.09							
40	2MAXI J0206+153	31.7	15.3	0.130	9.8	13.1±1.3	6.3	2.5±0.4	0.26±0.09	RXC J0206.3+1511	31.598	15.188	0.248	Galaxy Cluster	M	
41	2MAXI J0207+751	31.8	75.1	0.283	8.2	7.3±0.9	3.2	1.0±0.3	0.41±0.14							
42	2MAXI J0213-637	33.4	-63.8	0.223	10.0	6.9±0.7	5.5	1.4±0.3	0.22±0.10							
43	2MAXI J0224+186	36.1	18.6	0.080	12.0	14.3±1.2	9.6	3.5±0.4	0.14±0.07							
44	2MAXI J0228+314	37.1	31.4	0.103	12.3	18.0±1.5	10.9	4.3±0.4	0.15±0.06	NGC 931 (9)	37.060	31.312	0.0167	Sy1.5	BG	
45	2MAXI J0231-440	37.8	-44.1	0.171	8.6	10.5±1.2	9.4	3.7±0.4	-0.04±0.08	RXC J0232.2-4420	38.070	-44.347	0.2836	Galaxy Cluster	M	
46	2MAXI J0232-090	38.1	-9.1	0.167	7.9	9.2±1.2	8.7	3.1±0.4	-0.01±0.09							
47	2MAXI J0233+324	38.4	32.5	0.106	11.4	16.6±1.5	9.8	3.9±0.4	0.17±0.07	NGC 973	38.584	32.506	0.0162	Sy2	B	

TABLE 1 — CONTINUED

No.	Name	R.A.	Decl.	$\sigma_{\text{stat}}^{[a]}$	$\delta D_{4-10\text{keV}}$	$f_{4-10\text{keV}}^{[b]}$	(6)	(5)	(4)	(3)	MAXI	(10)				(11)				(12)				(13)				(14)				(15)				(16)				(17)			
												$f_{3-4\text{keV}}^{[c]}$	$\delta D_{3-4\text{keV}}$	HR	Name ^[d]	R.A.	Decl.	z	Type ^[e]	Flag ^[f]	Note ^[g]	Counterpart	Name ^[d]	R.A.	Decl.	z	Type ^[e]	Flag ^[f]	Note ^[g]	Counterpart	Name ^[d]	R.A.	Decl.	z	Type ^[e]	Flag ^[f]	Note ^[g]						
96	2MAXI J0442-271	70.5	-27.2	0.262	9.2	10.1±1.1	6.8	2.4±0.3	0.17±0.09	IRAS 04392-2713	70.344	-27.139	0.0835	Sy1.5	B																												
97	2MAXI J0443-288	70.8	28.8	0.131	9.7	11.8±1.2	4.7	1.7±0.4	0.38±0.10	UGC 03142	70.945	28.972	0.0217	Sy1	B																												
98	2MAXI J0447-207	71.9	-20.8	0.240	7.1	7.3±1.0	7.6	2.5±0.3	-0.02±0.10	RXC J0448.2-2028	72.051	-20.470	0.072	Galaxy Cluster	M																												
99	2MAXI J0449-094	72.4	-9.4	0.225	7.3	6.8±0.9	3.2	1.1±0.4	0.32±0.15																																		
100	2MAXI J0450-035	72.6	-3.5	0.137	10.9	13.2±1.2	6.8	2.5±0.4	0.28±0.08																																		
101	2MAXI J0451-585	72.9	-58.6	0.141	8.8	8.4±0.9	4.5	1.2±0.3	0.38±0.11																																		
102	2MAXI J0453-752	73.4	-75.3	0.123	19.0	13.4±0.7	15.6	4.1±0.3	0.03±0.04	ESO 033-G 002	73.996	-75.541	0.0181	Sy2	B																												
103	2MAXI J0453+070	73.4	7.0	0.148	8.3	10.0±1.2	25.8	10.3±0.4	-0.51±0.05																																		
104	2MAXI J0457-696	74.4	-69.6	0.075	19.0	15.0±0.8	9.8	2.6±0.3	0.31±0.05																																		
105	2MAXI J0502+247	75.6	24.7	0.113	13.6	16.2±1.2	8.1	3.1±0.4	0.27±0.07	V1062 Tau	75.615	24.756		Nova	B																												
106	2MAXI J0504-239	76.2	-24.0	0.163	8.0	8.8±1.1	3.1	1.0±0.3	0.47±0.13	2MASX J05054575-2351139	76.441	-23.854	0.035	Sy2 HII	B																												
107	2MAXI J0505-044	77.2	-4.4	0.209	7.1	7.6±1.1	3.5	1.2±0.4	0.34±0.14																																		
108	2MAXI J0509+677	77.5	67.8	0.104	12.4	10.8±0.9	11.6	3.5±0.3	0.01±0.06	87GB 050246.4+673341	76.984	67.623	0.314	QSO	B																												
109	2MAXI J0510+167	77.6	16.7	0.064	18.1	28.7±1.6	13.6	5.4±0.4	0.27±0.04																																		
110	2MAXI J0514-399	78.6	-40.0	0.022	53.6	78.2±1.5	51.5	24.6±0.5	0.02±0.01	NGC 1851 (30)	78.527	-40.044		LMXB/NS in globular c	BG	(D)																											
111	2MAXI J0515-616	78.9	-61.6	0.190	8.6	6.8±0.8	6.7	1.8±0.3	0.10±0.09																																		
112	2MAXI J0516-001	79.1	-0.1	0.064	18.4	20.8±1.1	16.9	6.3±0.4	0.04±0.04	Ark 120 (31)	79.048	-0.150	0.0323	Sy1	BG																												
113	2MAXI J0516-455	79.2	-45.6	0.151	9.4	12.6±1.3	7.6	3.0±0.4	0.16±0.08																																		
114	2MAXI J0516-102	79.2	-10.2	0.184	8.4	8.7±1.0	6.7	2.2±0.3	0.13±0.09	MCG -02-14-009	79.088	-10.562	0.0285	Sy1	B																												
115	2MAXI J0516+172	79.2	17.2	0.150	8.7	13.7±1.6	8.0	3.2±0.4	0.17±0.08	RXC J0516.3+1712	79.086	17.209	0.115	Galaxy Cluster	M																												
116	2MAXI J0517+065	79.4	6.5	0.141	9.2	11.0±1.2	12.5	4.8±0.4	-0.14±0.07	RXC J0516.6+0626	79.155	6.438	0.0284	Galaxy Cluster	M																												
117	2MAXI J0518-325	79.6	-32.5	0.123	8.3	9.4±1.1	7.4	2.7±0.4	0.07±0.09	ESO 362-18	79.899	-32.638	0.0125	Sy1.5	B																												
118	2MAXI J0520-719	80.1	-71.9	0.005	241.0	278.1±1.2	191.3	91.3±0.5	-0.00±0.00	LMC X-2 (32)	80.117	-71.965		LMXB/NS	BG																												
119	2MAXI J0522-631	80.6	63.2	0.147	8.8	8.7±1.0	7.9	2.4±0.3	0.08±0.08																																		
120	2MAXI J0523-363	80.8	-36.3	0.117	10.8	12.7±1.2	9.6	3.5±0.4	0.08±0.07	PKS 0521-36	80.742	-36.459	0.0553	BL Lac	BM																												
121	2MAXI J0529-327	82.3	-32.7	0.039	34.6	42.1±1.2	17.7	6.7±0.4	0.35±0.03	TV Col (33)	82.356	-32.818		CV/DQ Her	BG																												
122	2MAXI J0529-114	82.5	-11.5	0.143	7.6	7.7±1.0	9.1	3.0±0.3	-0.10±0.09																																		
123	2MAXI J0532-663	83.2	-66.4	0.013	93.8	91.2±1.0	51.2	16.7±0.3	0.28±0.01	LMC X-4 (34)	83.207	-66.371		HMXB/NS	BG																												
124	2MAXI J0533-024	83.4	-2.5	0.207	8.6	10.4±1.2	8.9	3.3±0.4	0.01±0.08																																		
125	2MAXI J0535-580	83.8	-58.1	0.067	16.1	14.9±0.9	10.0	2.9±0.3	0.26±0.05	TW Pic	83.711	-58.028																															
126	2MAXI J0535-052	83.8	-5.3	0.027	46.1	61.7±1.3	54.9	26.2±0.5	-0.13±0.01	Trapezium Cluster (35)	83.819	-5.387																															
127	2MAXI J0539-640	84.8	-64.1	0.007	146.4	170.7±1.2	194.4	100.5±0.5	-0.29±0.00	LMC X-3 (36)	84.735	-64.084																															
128	2MAXI J0539-696	85.0	-69.7	0.007	162.6	165.9±1.0	206.1	106.6±0.5	-0.32±0.00	LMC X-1 (37)	84.911	-69.743																															
129	2MAXI J0541-019	85.3	-2.0	0.098	13.9	16.9±1.2	16.1	6.2±0.4	-0.06±0.05																																		
130	2MAXI J0541-089	85.3	-8.9	0.172	7.3	7.2±1.0	2.2	0.7±0.3	0.52±0.17																																		
131	2MAXI J0542-407	85.6	-40.8	0.104	11.7	14.2±1.2	8.4	3.2±0.4	0.19±0.07	BVH2007/73	85.712	-41.001	0.642	Galaxy Cluster	M																												
132	2MAXI J0542+609	85.6	60.9	0.074	16.6	20.2±1.2	11.5	3.8±0.3	0.27±0.05	BY Cam (38)	85.704	60.859																															
133	2MAXI J0547-594	86.8	59.5	0.177	7.4	9.0±1.2	9.8	3.2±0.3	-0.05±0.08																																		
134	2MAXI J0549-621	87.5	-62.2	0.137	9.5	7.6±0.8	8.5	2.5±0.3	0.00±0.08																																		
135	2MAXI J0553-320	87.6	-32.0	0.071	13.9	21.9±1.6	17.3																																				

TABLE 1 — CONTINUED

(1)	(2)	MAXI	(3)	(4)	(5)	(6)	(7)	(8)	(9)	(10)	(11)	(12)	(13)	(14)	(15)	(16)	(17)
			Name	R.A.	Decl.	$\sigma_{\text{stat}}^{[a]}$	$\text{SD}_{4-10\text{keV}}$	$f_{4-10\text{keV}}^{[b]}$	$\text{SD}_{3-4\text{keV}}$	$f_{3-4\text{keV}}^{[c]}$	R.A.	Decl.	z	Type ^[e]	Flag ^[f]	Note ^[g]	
144	2MAXI J0607-352	91.9	-35.3	0.125	8.8	10.5 \pm 1.2	5.2	1.9 \pm 0.4	0.29 \pm 0.10	RXC J0605.8-3518	91.470	-35.301	0.1392	Galaxy Cluster	M		
145	2MAXI J0613-656	93.3	-65.7	0.177	8.9	6.4 \pm 0.7	10.2	2.7 \pm 0.3	-0.13 \pm 0.07						B		
146	2MAXI J0614-217	93.7	-21.8	0.136	8.9	9.5 \pm 1.1	7.5	2.4 \pm 0.3	0.12 \pm 0.09						B		
147	2MAXI J0615+712	94.0	71.3	0.167	8.2	7.2 \pm 0.9	1.6	0.4 \pm 0.3	0.69 \pm 0.17	Mrk 3	93.901	71.037	0.0135	Sy2	B		
148	2MAXI J0623-095	95.9	-9.6	0.156	7.9	8.4 \pm 1.1	2.2	0.7 \pm 0.3	0.59 \pm 0.16	SWIFT J062406.05-093855.0	96.025	-9.649		SRG/X-RAY	B		
149	2MAXI J0627-543	96.9	-54.3	0.075	10.5	25.5 \pm 2.4	25.9	10.0 \pm 0.4	-0.09 \pm 0.05	RXC J0627.2-5428 (42)	96.810	-54.470	0.0506	Galaxy Cluster	M		
150	2MAXI J0632+738	98.2	73.9	0.163	12.3	10.9 \pm 0.9	6.9	2.0 \pm 0.3	0.29 \pm 0.08						B		
151	2MAXI J0634-751	98.7	-75.2	0.142	8.3	6.8 \pm 0.8	7.6	1.9 \pm 0.2	0.08 \pm 0.09	PKS 0637-752	98.944	-75.271	0.651	Sy1	B		
152	2MAXI J0639+279	100.0	27.9	0.254	7.6	5.6 \pm 0.7	2.2	0.8 \pm 0.4	0.39 \pm 0.20						B		
153	2MAXI J0640-257	100.2	-25.7	0.216	7.6	7.8 \pm 1.0	7.8	2.6 \pm 0.3	-0.01 \pm 0.09	ESO 490-IG026	100.049	-25.895	0.0248				
154	2MAXI J0641-540	100.4	-54.0	0.123	9.4	9.7 \pm 1.0	10.1	3.1 \pm 0.3	0.02 \pm 0.07						B		
155	2MAXI J0644+554	101.2	55.4	0.115	12.0	13.9 \pm 1.2	6.3	2.2 \pm 0.4	0.34 \pm 0.08						BG		
156	2MAXI J0656-560	104.2	-56.1	0.093	11.5	12.2 \pm 1.1	9.6	2.8 \pm 0.3	0.17 \pm 0.07	Bullet Cluster	104.622	-55.953	0.296		BM		
157	2MAXI J0706-573	106.7	-57.3	0.195	7.4	4.8 \pm 0.6	3.8	1.1 \pm 0.3	0.18 \pm 0.14								
158	2MAXI J0707+641	106.9	64.1	0.205	7.1	6.6 \pm 0.9	7.5	2.2 \pm 0.3	-0.01 \pm 0.10	VIZW 118	106.805	64.600	0.0797		B		
159	2MAXI J0710+592	107.6	59.2	0.086	14.8	15.4 \pm 1.0	15.4	5.1 \pm 0.3	-0.00 \pm 0.05	2MASX J07103005+5908202 (43)	107.625	591.39	0.125	BL Lac	M		
160	2MAXI J0715-363	108.6	-36.4	0.298	8.1	9.7 \pm 1.2	11.5	4.3 \pm 0.4	-0.15 \pm 0.07	RXC J0717.1-3621	109.295	-36.360	0.032	Galaxy Cluster			
161	2MAXI J0715+442	109.0	44.3	0.113	11.1	14.8 \pm 1.3	9.8	3.9 \pm 0.4	0.11 \pm 0.07								
162	2MAXI J0717-494	109.3	-49.5	0.233	7.1	7.4 \pm 1.0	4.2	1.5 \pm 0.4	0.25 \pm 0.13						M		
163	2MAXI J0721+555	110.4	55.6	0.149	9.6	10.8 \pm 1.1	12.3	4.5 \pm 0.4	-0.12 \pm 0.07	RXC J0721.3+5547	110.343	55.786	0.0381	Galaxy Cluster			
164	2MAXI J0723-731	110.9	-73.2	0.146	9.7	7.5 \pm 0.8	6.6	1.6 \pm 0.3	0.20 \pm 0.09						B		
165	2MAXI J0730+100	112.7	10.0	0.111	10.5	14.0 \pm 1.3	4.2	1.7 \pm 0.4	0.47 \pm 0.10	BG CMi	112.871	9.940		CV/DQ Her	B		
166	2MAXI J0740+497	115.2	49.8	0.158	7.3	8.9 \pm 1.2	7.4	2.8 \pm 0.4	0.03 \pm 0.10						B		
167	2MAXI J0742-547	115.5	-54.7	0.205	9.1	8.7 \pm 1.0	7.5	2.2 \pm 0.3	0.12 \pm 0.09	2MASX J07410919-5447461	115.637	49.810	0.0222	Sy1.2	B		
168	2MAXI J0742+745	115.6	74.5	0.226	7.1	6.0 \pm 0.8	7.2	2.0 \pm 0.3	-0.02 \pm 0.10	RXC J0741.7+7414	115.437	74.248	0.2149	Galaxy Cluster	M		
169	2MAXI J0744+288	116.1	28.8	0.152	7.4	8.2 \pm 1.1	7.5	2.7 \pm 0.4	-0.01 \pm 0.09								
170	2MAXI J0745-530	116.3	-53.1	0.213	9.8	9.4 \pm 1.0	7.6	2.3 \pm 0.3	0.14 \pm 0.08	V0436 Car (44)	116.243	-52.952		CV/DQHer	G		
171	2MAXI J0751+149	117.8	15.0	0.091	12.4	21.2 \pm 1.7	6.3	3.0 \pm 0.5	0.40 \pm 0.08	PQ Gem	117.823	14.740		CV/DQ Her	B		
172	2MAXI J0751+182	117.9	18.2	0.171	8.4	9.6 \pm 1.2	6.9	2.6 \pm 0.4	0.10 \pm 0.09								
173	2MAXI J0752+221	118.2	22.2	0.353	8.1	6.2 \pm 0.8	4.6	1.6 \pm 0.4	0.11 \pm 0.12								
174	2MAXI J0758-632	119.6	63.2	0.248	7.2	6.9 \pm 1.0	7.3	2.2 \pm 0.3	0.01 \pm 0.10								
175	2MAXI J0801+162	120.3	16.2	0.141	8.0	10.6 \pm 1.3	7.3	2.8 \pm 0.4	0.11 \pm 0.09								
176	2MAXI J0804+052	121.0	5.2	0.144	8.0	9.7 \pm 1.2	2.5	0.9 \pm 0.4	0.55 \pm 0.14	Mrk 1210	121.024	5.114	0.0135	Sy2	B		
177	2MAXI J0808+757	122.2	13.4	0.134	9.0	8.5 \pm 0.9	10.4	3.0 \pm 0.3	-0.03 \pm 0.07	PG 0804+761	122.744	76.045	0.1	Sy1	B		
178	2MAXI J0814+627	123.7	62.7	0.114	8.2	8.4 \pm 1.0	8.7	2.7 \pm 0.3	0.01 \pm 0.08	MS0811.6+6301	123.999	62.886	0.312	Galaxy Cluster	M		
179	2MAXI J0815-572	124.0	-57.2	0.079	14.5	14.1 \pm 1.0	18.3	5.5 \pm 0.3	-0.09 \pm 0.04						MG		
180	2MAXI J0817-074	124.4	-7.4	0.026	31.2	32.5 \pm 1.0	26.4	9.9 \pm 0.4	0.04 \pm 0.02	RXC J0817.4-0730 (46)	124.352	-7.513	0.0704	Galaxy Cluster	MG		
181	2MAXI J0817+017	124.4	1.7	0.094	9.4	10.7 \pm 1.1	8.0	2.9 \pm 0.4	0.09 \pm 0.08								
182	2MAXI J0823+082	125.8	8.2	0.237	7.5	6.9 \pm 0.9	4.6	1.7 \pm 0.4	0.15 \pm 0.12								
183	2MAXI J0825+733	126.3	73.3	0.103	12.5	11.2 \pm 0.9	7.4	2.1 \pm 0.3	0.28 \pm 0.07								
184	2MAXI J0827-642	126.8	-64.3	0.187	7.8	6.2 \pm 0.8	6.7	1.8 \pm 0.3	0.07 \pm 0.10								
185	2MAXI J0831+660	127.8	66.0	0.173	7.2	6.4 \pm 0.9	9.3	2.7 \pm 0.3	-0.13 \pm 0.09	RXC J0830.9+6551	127.743	65.850	0.1818	Galaxy Cluster	M		
186	2MAXI J0831-701	127.9	-70.1	0.154	9.9	7.3 \pm 0.7	2.5	0.6 \pm 0.2	0.59 \pm 0.13								
187	2MAXI J0835-040	129.0	-4.1	0.159	8.0	9.4 \pm 1.2	6.2	2.2 \pm 0.4	0.17 \pm 0.10								
188	2MAXI J0839+485	129.8	48.5	0.122	10.3	12.5 \pm 1.2	6.4	2.4 \pm 0.4	0.25 \pm 0.09	E1 UMa	129.592	48.634		CV/DQ Her	B		
189	2MAXI J0840-125	130.0	-12.6	0.151	9.7	9.6 \pm 1.1	6.9	2.2 \pm 0.3	0.17 \pm 0.09	3C 206	129.961	-12.243		QSO	B		
190	2MAXI J0840-708	130.2	70.8	0.100	11.9	10.8 \pm 0.9	6.3	1.8 \pm 0.3	0.33 \pm 0.08	[HB89] 0836+710	130.351	-70.895	2.172	Bazar	BM		
191	2MAXI J0846-142	131.7	74.0	0.233	8.0	8.0 \pm 1.1	4.7	1.8 \pm 0.4	0.19 \pm 0.12	2MASX J0845.850+1420345	131.327	74.0	0.0606	Sy1.9	B		

TABLE 1 — CONTINUED

No.	Name	R.A.	Decl.	MAXI			(10)			(11)			(12)			(13)			(14)			(15)		
				$\sigma_{\text{stat}}^{[a]}$	$\sigma_{\text{syst}}^{[a]}$	$f_{D,4-10\text{keV}}$	$f_{4-10\text{keV}}^{[b]}$	$f_{3-4\text{keV}}^{[c]}$	$f_{D,3-4\text{keV}}$	HR	Name ^[d]	R.A.	Decl.	z	Type ^[e]	Flag ^[f]	Note ^[g]							
192	2MAXI J0854-074	133.6	-7.5	0.214	7.8	7.9±1.0	6.2	2.1±0.3	0.09±0.10	0.12±0.08	ABELL 754 (47)	137.209	-9.637	0.0542	Galaxy Cluster	BMG								
193	2MAXI J0856-247	134.0	-24.8	1.045	10.4	11.1±1.1	8.4	2.8±0.3	0.09±0.01	0.35±0.10	RXXC J0918.1-205 (48)	139.527	-12.093	0.0539	Galaxy Cluster	MG								
194	2MAXI J0909-096	137.3	-9.6	0.021	58.6	71.2±1.2	49.2	19.6±0.4	0.09±0.01	0.21±0.06	MCG -01-24-012	140.193	-8.056	0.0196	Galaxy Cluster	Sy2								
195	2MAXI J0910+524	137.7	52.5	0.194	9.5	11.5±1.2	5.1	1.8±0.4	0.35±0.10	-0.09±0.04	RXXC J1130.3-434	172.581	-14.583	0.1068	Galaxy Cluster	Sy1								
196	2MAXI J0918-119	139.5	-12.0	0.072	17.0	19.0±1.1	21.4	7.4±0.3	0.14±0.09	0.22±0.04	MCG +10-17-061	176.388	-58.978	0.0099	Galaxy Cluster	B								
197	2MAXI J0920-079	140.2	-7.9	0.092	14.7	17.0±1.2	10.3	3.6±0.4	0.21±0.06	0.22±0.04	DO Dra (59)	140.1±0.3	-14.469	0.0834	Galaxy Cluster	CV/DQ Her								
198	2MAXI J0921-224	140.4	-22.4	0.230	8.3	9.2±1.1	8.3	2.7±0.3	0.05±0.09	0.20±0.09	2MASX J1132.8+428	140.1±0.3	-14.321	0.1342	Galaxy Cluster	BL Lac								
199	2MAXI J0922+301	140.6	30.1	0.239	7.1	8.6±1.2	5.2	1.9±0.4	0.18±0.12	0.20±0.09	2MASX J1136.009+6737042 (57)	140.929	-22.909	0.0323	Galaxy Cluster	Sy1.2								
200	2MAXI J0923+228	140.8	22.9	0.130	9.2	10.3±1.1	6.5	2.3±0.4	0.20±0.09	0.18±0.04	DO Dra (60)	141.1±0.3	-14.367	0.0214	Galaxy Cluster	BL Lac								
201	2MAXI J0923+521	141.0	52.1	0.074	17.0	20.7±1.2	15.2	5.7±0.4	0.09±0.04	0.18±0.01	NGC 2992	146.425	-14.326	0.0077	Galaxy Cluster	Sy2								
202	2MAXI J0924-316	141.0	-31.6	0.025	47.5	63.5±1.3	46.2	20.2±0.4	0.01±0.02	0.18±0.01	NGC 2992	146.425	-14.326	0.0077	Galaxy Cluster	Sy1.9								
203	2MAXI J0945-140	146.5	-14.1	0.145	9.5	9.2±1.0	4.2	1.3±0.3	0.39±0.11	0.18±0.13	NGC 2992	146.425	-14.326	0.0077	Galaxy Cluster	Sy2								
204	2MAXI J0947+288	146.9	28.9	0.191	7.1	8.2±1.2	4.2	1.5±0.4	0.28±0.13	0.18±0.01	MCG -05-23-016 (50)	146.917	-30.949	0.0085	Galaxy Cluster	BL Lac								
205	2MAXI J0947-308	146.9	-30.9	0.020	62.0	82.9±1.3	43.2	18.9±0.4	0.18±0.01	0.18±0.01	MCG -05-23-016 (50)	146.917	-30.949	0.0085	Galaxy Cluster	BL Lac								
206	2MAXI J0949+757	147.3	75.7	0.255	7.3	6.5±0.9	6.3	1.8±0.3	0.09±0.10	0.18±0.01	NGC 2992	146.425	-14.326	0.0077	Galaxy Cluster	Sy2								
207	2MAXI J0953-763	148.4	-76.3	0.161	9.8	7.7±0.8	7.4	1.9±0.3	0.15±0.08	0.15±0.08	NGC 2992	146.425	-14.326	0.0077	Galaxy Cluster	BL Lac								
208	2MAXI J0955-694	148.8	-69.4	0.282	9.1	7.3±0.8	4.9	1.3±0.3	0.31±0.11	0.18±0.01	NGC 2992	146.425	-14.326	0.0077	Galaxy Cluster	Sy1								
209	2MAXI J0956+694	149.2	69.4	0.048	27.6	24.2±0.9	22.9	7.1±0.3	0.05±0.03	0.05±0.03	NGC 2992	146.425	-14.326	0.0077	Galaxy Cluster	Sy1								
210	2MAXI J1000-313	150.2	-31.3	0.091	13.3	14.3±1.1	8.6	3.1±0.4	0.19±0.07	0.19±0.07	NGC 2992	146.425	-14.326	0.0077	Galaxy Cluster	Sy1								
211	2MAXI J1007+662	151.8	66.3	0.198	8.3	6.5±0.8	4.2	1.2±0.3	0.27±0.12	0.27±0.12	NGC 2992	146.425	-14.326	0.0077	Galaxy Cluster	Sy1								
212	2MAXI J1009-311	152.4	-31.2	0.098	13.9	16.8±1.2	13.6	5.0±0.4	0.05±0.05	0.05±0.05	NGC 2992	146.425	-14.326	0.0077	Galaxy Cluster	Sy1								
213	2MAXI J1016-274	154.1	-27.5	0.213	8.7	9.4±1.1	6.7	2.4±0.4	0.13±0.09	0.13±0.09	NGC 3227 (52)	155.877	-19.865	0.0039	Galaxy Cluster	BL Lac								
214	2MAXI J1020-034	155.1	-3.4	0.165	8.2	9.6±1.2	9.0	3.2±0.4	-0.00±0.08	0.00±0.08	NGC 333-038	155.627	-50.102	0.158	Galaxy Cluster	Sy1.5								
215	2MAXI J1023+199	155.9	19.9	0.064	19.5	23.2±1.2	15.8	5.8±0.4	0.14±0.04	0.14±0.04	NGC 333-038	158.598	-73.014	0.022	Galaxy Cluster	Galaxy								
216	2MAXI J1025+499	156.3	49.9	0.250	7.1	8.6±1.2	8.5	3.1±0.4	-0.05±0.09	0.05±0.09	RXXC J1022.5+5006	155.418	-3.454	0.0408	Galaxy Cluster	Sy1								
217	2MAXI J1028+729	157.2	73.0	0.202	7.5	7.0±0.9	3.4	0.9±0.3	0.41±0.13	0.41±0.13	NGC 333-038	155.877	-19.865	0.0039	Galaxy Cluster	Sy1.5								
218	2MAXI J1030-351	157.7	-35.2	0.140	8.9	10.8±1.2	12.4	4.5±0.4	-0.12±0.07	0.12±0.07	NGC 333-038	155.627	-50.102	0.158	Galaxy Cluster	Galaxy								
219	2MAXI J1031-143	158.0	-14.3	0.109	11.1	11.7±1.1	7.6	2.4±0.3	0.22±0.08	0.22±0.08	2MASI J1031543-141651	157.976	-14.281	0.086	Galaxy Cluster	Sy1								
220	2MAXI J1036-275	159.1	-27.6	0.046	26.5	32.1±1.2	36.8	14.6±0.4	-0.16±0.02	0.16±0.02	RXXC J1036.6-2731 (53)	159.174	-27.524	0.0126	Galaxy Cluster	BL Lac								
221	2MAXI J1037-104	159.4	-10.5	0.223	7.1	6.8±1.0	7.5	2.5±0.3	-0.05±0.10	0.05±0.10	NGC 333-038	155.877	-19.865	0.0039	Galaxy Cluster	Sy1								
222	2MAXI J1103-234	165.8	-23.4	0.105	12.3	13.8±1.1	17.8	6.2±0.3	-0.15±0.05	0.15±0.05	2MASX J113765-2329307 (54)	165.907	-23.492	0.186	Galaxy Cluster	BL Lac								
223	2MAXI J1104+382	166.1	38.2	0.011	107.1	182.2±1.7	111.4	70.9±0.6	-0.09±0.01	0.09±0.01	Mk421 (55)	166.114	-38.209	0.03	Galaxy Cluster	BL Lac								
224	2MAXI J1105+244	166.4	72.4	0.048	24.6	24.8±1.0	13.8	4.1±0.3	0.33±0.04	0.33±0.04	NGC 3516 (56)	166.698	-72.569	0.0088	Galaxy Cluster	Sy1.5								
225	2MAXI J1108-056	167.1	-5.6	0.216	7.2	7.9±1.1	5.0	1.8±0.4	0.19±0.12	0.19±0.12	NGC 3516 (56)	166.698	-72.569	0.0088	Galaxy Cluster	Sy1								
226	2MAXI J1116-768	169.2	-76.8	0.173	9.3	7.2±0.8	12.7	3.2±0.3	-0.16±0.07	0.16±0.07	NGC 3516 (56)	166.698	-72.569	0.0088	Galaxy Cluster	Sy1								
227	2MAXI J1123+120	170.9	12.0	0.325	8.4	6.7±0.8	5.9	2.2±0.4	0.00±0.10	0.00±0.10	NGC 3516 (56)	166.698	-72.569	0.0088	Galaxy Cluster	Sy1								
228	2MAXI J1127+190	171.8	19.0	0.209	7.9	7.3±0.9	4.9	1.7±0.4	0.17±0.12	0.17±0.12	2MASX J11271632+1909198	171.818	-19.156	0.1055	Galaxy Cluster	Sy1								
229	2MAXI J1129-144	172.3	-14.5	0.096	11.6	12.6±1.1	9.1	3.0±0.3	0.16±0.07	0.16±0.07	RXXC J1130.3-434	172.581	-14.583	0.1068	Galaxy Cluster	Sy1								
230	2MAXI J1132+146	173.1	14.6	0.138	8.8	10.4±1.2	8.3	3.2±0.4	0.04±0.08	0.04±0.08	RXXC J1132.8+428	173.221	-14.469	0.0834	Galaxy Cluster	BL Lac								
231	2MAXI J1136-675	174.0	67.6	0.090	15.2	14.4±0.9	16.9	5.1±0.3	-0.04±0.04	0.04±0.04	NGC 3516 (56)	173.221	-14.469	0.0834	Galaxy Cluster	BL Lac								
232	2MAXI J1138-119	174.7	-11.9	0.286	7.5	7.3±1.0	6.1	2.0±0.3	0.09±0.10	0.09±0.10	NGC 3516 (56)	173.221	-14.469	0.0834	Galaxy Cluster	BL Lac								
233	2MAXI J1139-220	174.8	22.1	0.155	9.0	9.2±1.0	5.4	1.9±0.4	0.23±0.10	0.23±0.10	NGC 3516 (56)	173.221	-14.469	0.0834	Galaxy Cluster	BL Lac								
234	2MAXI J1139-376	174.9	-37.7	0.040	29.7	39.7±1.3	21.6	8.4±0.4	0.23±0.03	0.23±0.03	NGC 3783 (58)	174.757	-37.739	0.0097	Galaxy Cluster	Sy1								
235	2MAXI J1143-592	175.9	59.2	0.187	8.3	9.9±1.2	7.7	2.4±0.3	0.14±0.09	0.14±0.09	MCG +10-17-061	176.388	-58.978	0.0099	Galaxy Cluster	BL Lac								
236	2MAXI J1144+717	176.0	71.7	0.059	20.4	20.1±1.0	14.1	4.2±0.3	0.22±0.04	0.22±0.04	DO Dra (59)	175.910	-71.689	0.0214	Galaxy Cluster	BL Lac								
237	2MAXI J1144+198	176.2	19.8	0.052	24.5	28.9±1.2	31.1	12.4±0.4	-0.13±0.03	0.13±0.03	A1367 (60)	176.152	-19.759	0.0214	Galaxy Cluster	BL Lac								
238	2MAXI J1145-182	176.4	-18.2	0.068	15.0	16.2±1.1	12.7	4.1±0.3	0.13±0.05	0.13±0.05	NGC 3516 (56)	176.152	-19.759	0.0214	Galaxy Cluster	BL Lac								
239	2MAXI J1149-077	177.4	-7.8	0.192	7.1	7.6±1.1	6.4	2.2±0.4	0.05±0.11	0.05±0.11	NGC 3516 (56)	176.152	-19.759	0.0214	Galaxy Cluster	BL Lac								

TABLE 1 — CONTINUED

(1)	(2)	MAXI	(3)	(4)	(5)	(6)	(7)	(8)	(9)	(10)	(11)	(12)	(13)	(14)	(15)	(16)	(17)	
			No.	Name	R.A.	Decl.	$\sigma_{\text{stat}}^{[a]}$	$\text{SD}_{4-10\text{keV}}$	$f_{4-10\text{keV}}^{[b]}$	$\text{SD}_{3-4\text{keV}}$	$f_{3-4\text{keV}}^{[c]}$	HR	Name ^[d]	R.A.	Decl.	z	Type ^[e]	Flag ^[f]
240	2MAXI J1151-119	177.8	-11.9	0.155	9.1	9.3±1.0	6.8	2.3±0.3	0.14±0.09	12.2	4.5±0.4	-0.04±0.06	RXC J1155.3+2324	178.827	23.407	0.1427	Galaxy Cluster	M
241	2MAXI J1155+234	178.8	23.5	0.135	10.7	12.6±1.2	7.3	2.5±0.3	0.03±0.09	RXC J1200.3+5613	180.092	56.230	0.065	Galaxy Cluster	M			
242	2MAXI J1158+562	179.7	56.3	0.177	8.0	8.2±1.0	8.5	2.7±0.3	0.01±0.09	NGC 4051	180.790	44.531	0.0023	Sy1.5	B			
243	2MAXI J1159-307	179.9	-30.8	0.192	7.0	8.5±1.2	8.5	2.7±0.3	0.08±0.05	NGC 4051	180.400	40.015	0.40±0.15	NGC 4151 (62)	BG			
244	2MAXI J1203+446	180.8	44.6	0.121	15.5	18.8±1.2	13.1	5.2±0.4	0.08±0.05	NGC 4235	182.636	39.406	0.0033	Sy1.5	B			
245	2MAXI J1209+476	182.4	47.6	0.200	7.3	8.0±1.1	3.1	1.1±0.4	0.45±0.01	NGC 4235	184.291	7.192	0.008	IC 4329A (80)	BM			
246	2MAXI J1210+394	182.7	39.4	0.015	91.8	122.6±1.3	31.6	15.1±0.5	0.24±0.09	NGC 4235	186.737	39.839	0.0235	Galaxy Cluster	M			
247	2MAXI J1217+073	184.4	7.3	0.124	9.3	11.3±1.2	6.1	2.3±0.4	0.24±0.09	NGC 4235	188.730	7.074	0.0235	Sy1.4	B			
248	2MAXI J1219-036	184.8	3.7	0.102	13.8	16.7±1.2	14.9	5.7±0.4	-0.02±0.05	NGC 4235	190.730	2.161	0.016	NGC 4235	BM			
249	2MAXI J1220+300	185.0	30.1	0.046	25.7	34.4±1.3	25.3	10.1±0.4	0.06±0.03	NGC 4235	185.433	75.311	0.0708	BL Lac	BM			
250	2MAXI J1220+752	185.2	75.3	0.132	10.8	7.7±0.7	7.0	2.0±0.3	0.12±0.08	NGC 4235	186.995	-48.896	CV?	CV?	B			
251	2MAXI J1227-091	186.9	-9.1	0.197	8.3	9.2±1.1	5.1	1.7±0.3	0.27±0.11	NGC 4235	187.706	-12.391	0.00436	Galaxy Cluster	G			
252	2MAXI J1228-486	187.1	-48.6	0.094	14.2	17.2±1.2	9.8	3.7±0.4	0.21±0.06	NGC 4235	189.569	-38.713	0.00436	CV/DQ HER	BG			
253	2MAXI J1229-021	187.3	2.2	0.021	61.4	82.1±1.3	44.3	19.4±0.4	0.16±0.01	NGC 4235	190.104	-11.793	0.193	Galaxy Cluster	M			
254	2MAXI J1230+124	187.6	12.5	0.010	124.3	196.4±1.6	145.2	104.0±0.7	-0.24±0.00	NGC 4235	192.200	-41.308	0.0114	Virgo galaxy cluster (65)	MG			
255	2MAXI J1237-387	189.4	-38.7	0.093	13.9	16.9±1.2	10.0	3.7±0.4	0.19±0.06	NGC 4235	193.925	-12.655	0.0585	Galaxy Cluster	M			
256	2MAXI J1240-049	190.0	-5.0	0.083	16.3	18.7±1.1	12.6	4.7±0.4	0.14±0.05	NGC 4235	194.320	-6.701	0.1962	Galaxy Cluster	M			
257	2MAXI J1240-116	190.2	-11.7	0.211	7.3	8.1±1.1	3.8	1.3±0.3	0.36±0.13	NGC 4235	194.290	-17.400	0.0473	Galaxy Cluster	MG			
258	2MAXI J1249-412	192.3	-41.2	0.015	64.1	93.4±1.5	70.2	36.3±0.5	-0.09±0.01	NGC 4235	194.320	-30.377	0.0554	Galaxy Cluster	M			
259	2MAXI J1252-291	193.2	-29.2	0.021	57.9	84.5±1.5	53.9	23.6±0.4	0.08±0.01	NGC 4235	195.511	-6.701	0.1962	Galaxy Cluster	MG			
260	2MAXI J1253-127	193.4	-12.7	0.233	7.5	7.9±1.0	5.1	1.7±0.3	0.21±0.11	NGC 4235	196.320	-17.400	0.0473	Galaxy Cluster	M			
261	2MAXI J1254-063	193.5	-6.4	0.230	8.7	9.2±1.1	5.2	1.8±0.4	0.24±0.11	NGC 4235	197.420	-17.400	0.0473	Galaxy Cluster	MG			
262	2MAXI J1256-305	194.2	-30.6	0.103	10.9	14.5±1.3	17.5	6.7±0.4	-0.17±0.05	NGC 4235	198.840	-4.195	0.0845	Galaxy Cluster	M			
263	2MAXI J1257-173	194.3	-17.4	0.056	20.4	22.8±1.1	23.1	8.0±0.3	-0.03±0.03	NGC 4235	199.953	-27.981	0.0231	Galaxy Cluster	MG			
264	2MAXI J1258+016	194.6	1.6	0.167	7.3	8.0±1.1	6.7	2.4±0.4	0.05±0.10	NGC 4235	201.365	-43.019	0.0231	Galaxy Cluster	MG			
265	2MAXI J1259-043	194.8	-4.4	0.068	21.0	23.5±1.1	18.0	6.7±0.4	0.07±0.04	NGC 4235	201.725	-27.183	0.0458	Galaxy Cluster	M			
266	2MAXI J1259-279	194.9	28.0	0.007	161.1	254.4±1.6	121.5	77.4±0.6	0.04±0.01	NGC 4235	202.429	-31.602	0.0488	Galaxy Cluster	MG			
267	2MAXI J1259-017	194.9	-1.7	0.089	14.7	17.3±1.2	16.7	6.2±0.4	-0.04±0.05	NGC 4235	203.974	-34.296	0.0077	Galaxy Cluster	BG			
268	2MAXI J1304+192	196.2	19.3	0.173	7.4	8.5±1.2	8.7	3.1±0.4	-0.05±0.09	NGC 4235	204.566	4.543	0.023	Galaxy Cluster	BG			
269	2MAXI J1307-400	196.9	-40.0	0.129	10.0	12.2±1.2	2.7	1.0±0.4	0.60±0.12	NGC 4235	206.875	-11.749	0.4516	Galaxy Cluster	M			
270	2MAXI J1311-014	198.0	-1.5	0.103	13.1	15.4±1.2	13.1	4.8±0.4	0.03±0.05	NGC 4235	207.221	26.596	0.0622	Galaxy Cluster	MG			
271	2MAXI J1325-429	201.4	-43.0	0.007	164.7	300.2±1.8	66.0	34.1±0.5	0.48±0.01	Cen A (72)	207.330	-30.309	0.016	Galaxy Cluster	BMG			
272	2MAXI J1327-272	201.8	-27.2	0.074	17.4	20.0±1.2	18.0	6.4±0.4	0.01±0.04	NGC 4235	208.712	-27.183	0.0458	Galaxy Cluster	M			
273	2MAXI J1329-315	202.4	-31.5	0.025	52.1	63.3±1.2	51.8	22.7±0.4	-0.04±0.01	NGC 4235	209.940	19.271	0.0643	Galaxy Cluster	M			
274	2MAXI J1332+593	203.0	59.3	0.184	8.1	8.2±1.0	10.1	3.2±0.3	-0.99±0.08	NGC 4235	210.440	-2.333	0.0488	Galaxy Cluster	M			
275	2MAXI J1335-341	203.9	-34.2	0.044	30.7	36.2±1.2	21.9	8.7±0.4	0.15±0.03	NGC 4235	211.440	-2.333	0.0488	Galaxy Cluster	BMG			
276	2MAXI J1338-046	204.6	4.6	0.058	18.6	22.4±1.2	9.7	3.5±0.4	0.36±0.05	NGC 4235	212.040	-2.333	0.0488	Galaxy Cluster	BMG			
277	2MAXI J1347-328	206.9	-32.8	0.014	65.6	87.7±1.3	59.7	26.1±0.4	0.05±0.01	NGC 4235	212.540	-32.866	0.0391	Galaxy Cluster	B			
278	2MAXI J1348+024	207.1	2.4	0.173	8.3	9.0±1.1	2.8	0.9±0.3	0.52±0.14	NGC 4235	213.040	2.312	0.2312	Galaxy Cluster	M			
279	2MAXI J1348-117	207.2	-11.7	0.142	9.2	10.2±1.1	6.4	2.1±0.3	0.23±0.09	NGC 4235	213.540	-11.749	0.4516	Galaxy Cluster	MG			
280	2MAXI J1348+267	207.2	26.7	0.034	35.8	41.8±1.2	35.7	14.2±0.4	-0.02±0.02	NGC 4235	214.040	-2.333	0.0488	Galaxy Cluster	BMG			
281	2MAXI J1349-302	207.3	-30.2	0.021	62.3	75.7±1.2	47.1	18.7±0.4	0.14±0.01	NGC 4235	214.540	-30.309	0.016	Galaxy Cluster	Sy1.2			
282	2MAXI J1355-739	208.4	-73.9	0.062	9.9	7.7±0.8	5.8	1.5±0.3	0.24±0.09	NGC 4235	215.040	-73.9	0.016	Galaxy Cluster	Sy1.2			
283	2MAXI J1357+214	209.3	21.5	0.209	8.0	8.4±1.1	2.2	0.8±0.3	0.57±0.16	NGC 4235	215.540	-21.5	0.016	Galaxy Cluster	Sy1.2			
284	2MAXI J1357-094	209.3	-9.5	0.191	7.9	8.6±0.9	6.2	2.1±0.3	0.15±0.10	NGC 4235	216.040	-9.5	0.016	Galaxy Cluster	Sy1.2			
285	2MAXI J1358-478	209.7	-47.9	0.058	20.3	27.2±1.3	21.0	8.4±0.4	0.03±0.03	NGC 4235	216.540	-47.839	0.074	Galaxy Cluster	M			
286	2MAXI J1400+032	210.1	3.2	0.119	10.6	11.4±1.1	9.7	3.4±0.4	0.04±0.07	NGC 4235	217.040	-3.038	0.0235	Galaxy Cluster	B			
287	2MAXI J1406-300	211.7	-30.0	0.180	7.9	8.6±1.1	4.6	1.5±0.3	0.29±0.12	NGC 4235	217.540	-30.309	0.016	Galaxy Cluster	Sy1.4			

TABLE 1 — CONTINUED

1)	MAXI			(2)			(3)			(4)			(5)			(6)			(7)			(8)			(9)			(10)			(11)			Counterpart			(12)			(13)			(14)			(15)			(16)			(17)		
	Name	R.A.	Decl.	$\sigma_{\text{stat}}^{[a]}$	$\sigma_{\text{syst}}^{[a]}$	SD-4-10keV	$f_{4-10\text{keV}}^{[b]}$	SD-3-4keV	$f_{3-4\text{keV}}^{[c]}$	HR	Name ^[d]	R.A.	Decl.	z	Type ^[e]	Flag ^[f]	Note ^[g]																																					
288	2MAXI J1408-508	212.0	-50.9	0.058	20.7	22.3±1.1	18.0	6.3±0.4	0.07±0.04	RXC J1407.8-5100 (82)	211.969	-51.009	0.0966	Galaxy Cluster	MG																																							
289	2MAXI J1409-428	212.5	-42.8	0.124	9.9	13.3±1.3	9.2	3.5±0.4	0.11±0.07	RXC J1410.4-4246	212.619	-42.777	0.049	Galaxy Cluster	M																																							
290	2MAXI J1413-030	213.3	-3.1	0.026	49.6	60.3±1.2	32.1	12.5±0.4	0.22±0.02	NGC 5506 (83)	213.312	-3.208	0.0062	Galaxy Cluster	BG																																							
291	2MAXI J1417+253	214.4	25.3	0.063	19.8	28.8±1.5	20.6	8.1±0.4	0.08±0.03	NGC 5548 (84)	214.498	25.137	0.0172	Galaxy Cluster	BG																																							
292	2MAXI J1417+128	214.5	-12.9	0.300	7.2	6.0±0.8	3.2	1.0±0.3	0.31±0.15	ESO 511-G030	214.843	-26.645	0.0224	Galaxy Cluster	Sy1																																							
293	2MAXI J1419-265	214.9	-26.6	0.103	9.2	10.1±1.1	5.6	0.9±0.2	0.28±0.10	ESO 511-G030	216.095	24.614	0.0169	Galaxy Cluster	Sy2																																							
294	2MAXI J1420-779	215.1	-78.0	0.071	8.1	6.8±0.8	4.4	0.9±0.2	0.41±0.11	BL Lac	217.136	42.672	0.129	BL Lac	BMG																																							
295	2MAXI J1420+483	215.2	48.3	0.186	8.9	10.8±1.2	8.9	3.3±0.4	0.04±0.08	Galaxy Cluster	219.092	58.794	0.0314	Galaxy Cluster	Sy1.5																																							
296	2MAXI J1420-485	215.2	-48.6	0.195	9.7	10.7±1.1	7.7	2.8±0.4	0.11±0.08	Galaxy Cluster	219.269	37.971	0.163	Galaxy Cluster	M																																							
297	2MAXI J1422-380	215.7	-38.1	0.193	9.3	11.2±1.2	11.8	4.4±0.4	-0.09±0.07	BVH2007 NS 10	216.095	24.614	0.0169	Galaxy Cluster	Sy2																																							
298	2MAXI J1423+379	215.9	37.9	0.163	9.4	12.6±1.3	11.5	4.6±0.4	-0.05±0.07	NGC 5610	216.095	24.614	0.0169	Galaxy Cluster	B																																							
299	2MAXI J1423+250	216.0	25.0	0.179	7.7	11.2±1.5	5.8	2.1±0.4	0.27±0.10	NGC 5610	216.095	24.614	0.0169	Galaxy Cluster	M																																							
300	2MAXI J1428-730	217.1	-73.0	0.062	9.0	7.0±0.8	7.5	1.8±0.2	0.11±0.09	IES 1426+428 (85)	217.136	42.672	0.129	IES 1426+428 (85)	IES 1426+428 (85)																																							
301	2MAXI J1429+425	217.4	42.5	0.078	14.2	18.9±1.3	15.3	6.7±0.4	-0.04±0.05	IES 1426+428 (85)	217.136	42.672	0.129	IES 1426+428 (85)	IES 1426+428 (85)																																							
302	2MAXI J1436-364	219.1	-36.4	0.106	12.4	14.5±1.2	7.2	2.6±0.4	0.30±0.07	NGC 5610	216.095	24.614	0.0169	Galaxy Cluster	M																																							
303	2MAXI J1437+588	219.4	58.8	0.152	10.0	9.6±1.0	8.5	2.7±0.3	0.07±0.08	Mrk 817	219.092	58.794	0.0314	Galaxy Cluster	Sy1.5																																							
304	2MAXI J1441-386	220.3	-38.6	0.198	7.1	8.4±1.2	5.2	1.9±0.4	0.18±0.12	Galaxy Cluster	219.092	58.794	0.0314	Galaxy Cluster	M																																							
305	2MAXI J1446+152	221.6	15.3	0.176	9.8	11.9±1.2	7.8	2.9±0.4	0.14±0.08	Galaxy Cluster	219.092	58.794	0.0314	Galaxy Cluster	Sy1.5																																							
306	2MAXI J1454-243	223.6	-24.3	0.143	9.0	9.8±1.1	10.7	3.6±0.3	-0.06±0.07	NGC 5610	216.095	24.614	0.0169	Galaxy Cluster	M																																							
307	2MAXI J1455-381	223.9	-38.1	0.156	9.1	9.8±1.1	7.1	2.5±0.4	0.11±0.09	RXC J1456.2-3826	224.051	-38.440	0.115	Galaxy Cluster	M																																							
308	2MAXI J1459+217	224.9	21.7	0.160	9.2	10.4±1.1	11.1	3.9±0.4	-0.07±0.07	A2009	225.085	21.362	0.153	Galaxy Cluster	M																																							
309	2MAXI J1503-421	225.8	-42.1	0.099	12.4	15.0±1.2	12.4	5.6±0.4	0.19±0.06	NGC 5610	226.032	-2.805	0.2153	Galaxy Cluster	M																																							
310	2MAXI J1503+108	225.8	10.9	0.103	12.8	15.6±1.2	9.6	3.5±0.4	0.07±0.06	RXC J1504.1-0248	226.032	-2.805	0.2153	Galaxy Cluster	M																																							
311	2MAXI J1503-027	226.0	-2.7	0.090	12.4	14.5±1.2	11.7	4.1±0.4	0.07±0.06	NGC 5610	226.032	-2.805	0.2153	Galaxy Cluster	M																																							
312	2MAXI J1510-815	227.7	-81.5	0.119	9.0	7.4±0.8	3.4	0.9±0.3	0.47±0.12	2MASX J15144217-8123377	228.675	-81.394	0.0684	Galaxy Cluster	B																																							
313	2MAXI J1511+059	227.8	5.9	0.025	48.3	64.5±1.3	42.8	18.7±0.4	0.06±0.02	NGC 5610	228.675	-81.394	0.0684	Galaxy Cluster	B																																							
314	2MAXI J1512-213	228.0	-21.4	0.127	9.7	10.3±1.1	7.7	2.5±0.3	0.14±0.08	NGC 5610	228.675	-81.394	0.0684	Galaxy Cluster	Sy1.2																																							
315	2MAXI J1513+423	228.4	42.4	0.219	7.4	8.9±1.2	5.0	2.0±0.4	0.19±0.12	NGC 5610	228.673	-81.394	0.0684	Galaxy Cluster	Sy2																																							
316	2MAXI J1521+082	230.4	8.2	0.091	21.8	24.1±1.1	20.5	9.0±0.4	-0.06±0.03	NGC 5610	228.673	-81.394	0.0684	Galaxy Cluster	M																																							
317	2MAXI J1522+278	230.6	27.9	0.070	17.6	21.1±1.2	19.3	7.3±0.4	-0.03±0.04	RXC J1522.4+2742 (88)	230.610	27.709	0.0723	Galaxy Cluster	MG																																							
318	2MAXI J1523+304	230.8	30.5	0.119	11.5	13.5±1.2	12.6	4.9±0.4	-0.05±0.06	NGC 5610	230.610	27.709	0.0723	Galaxy Cluster	MG																																							
319	2MAXI J1523-300	231.0	-30.1	0.314	8.2	8.6±1.1	4.9	1.7±0.3	0.26±0.11	NGC 5610	230.610	27.709	0.0723	Galaxy Cluster	Sy1																																							
320	2MAXI J1535+581	233.9	58.1	0.143	8.1	8.0±1.0	7.2	2.3±0.3	0.06±0.09	NGC 5610	230.610	27.709	0.0723	Galaxy Cluster	Sy1																																							
321	2MAXI J1539-031	234.8	-3.2	0.127	11.6	13.6±1.2	8.8	3.1±0.3	0.18±0.07	RXC J1540.1-0318	234.910	-3.308	0.1533	Galaxy Cluster	M																																							
322	2MAXI J1539+219	234.9	22.0	0.159	8.3	8.9±1.1	8.3	2.9±0.4	0.01±0.09	A2107	234.910	21.789	0.0411	Galaxy Cluster	M																																							
323	2MAXI J1545+361	236.5	36.2	0.209	7.5	9.1±1.2	8.4	3.3±0.4	-0.05±0.09	A2124	234.910	-83.592	0.0728	Galaxy Cluster	M																																							
324	2MAXI J1546-834	236.6	-83.4	0.159	7.6	6.1±0.8	10.0	2.7±0.3	-0.16±0.08	RXC J1539.5-8335	234.910	-83.592	0.0728	Galaxy Cluster	Sy2																																							
325	2MAXI J1548-136	237.1	-13.6	0.092	13.3	13.9±1.0	8.0	2.6±0.3	0.27±0.07	NGC 5610	234.910	-13.758	0.0252	Galaxy Cluster	B																																							
326	2MAXI J1551-224	238.0	-22.5	0.167	8.8	9.0±1.0	5.0	1.7±0.3	0.28±0.11	NGC 5610	234.910	-13.758	0.0252	Galaxy Cluster	B																																							
327	2MAXI J1552+850	238.2	85.1																																																			

TABLE 1 — CONTINUED

(1)	(2)	(3)	(4)	(5)	(6)	(7)	(8)	(9)	(10)	(11)	(12)	(13)	(14)	(15)	(16)	(17)	
No.	Name	R.A.	Decl.	$\sigma_{\text{stat}}^{[a]}$	SD-4-10keV	$f_{4-10\text{keV}}^{[b]}$	SD-3-4keV	$f_{3-4\text{keV}}^{[c]}$	HR	Name ^[d]	Counterpart	R.A.	Decl.	z	Type ^[e]	Flag ^[f]	Note ^[g]
432	2MAXI J0424+751	310.7	75.2	0.055	22.9	21.4±0.9	17.4	5.2±0.3	0.15±0.04	4C+74.26 (129)	310.655	75.134	0.104	Sy1	BG		
433	2MAXI J0433-324	310.8	-32.5	0.194	7.2	7.2±1.0	10.2	3.7±0.4	-0.22±0.08								
434	2MAXI J0433-714	310.9	-71.4	0.212	8.0	6.9±0.9	8.0	2.0±0.3	0.06±0.09								
435	2MAXI J0444-106	311.1	-10.6	0.035	36.1	42.5±1.2	31.4	11.6±0.4	0.09±0.02	Mk 509 (130)	311.041	-10.723	0.0344	Sy1.2	BG		
436	2MAXI J12107-217	316.8	-21.7	0.123	8.9	7.7±0.9	6.3	2.0±0.3	0.11±0.10								
437	2MAXI J12108-439	317.1	-43.9	0.230	7.8	9.5±1.2	3.2	1.2±0.4	0.44±0.14	CD Ind							
438	2MAXI J12114-588	318.6	-58.9	0.130	9.3	8.2±0.9	7.5	2.1±0.3	0.13±0.08	2MASX J21140128+8204483	318.505	82.080	0.084	CV/AM HER	B		
439	2MAXI J12115+821	318.8	82.1	0.137	10.1	9.6±0.9	9.3	2.7±0.3	0.07±0.07	4U 2129+12 (131)	322.493	12.167		LMXB in globular clus	B		
440	2MAXI J12130+122	322.5	12.2	0.011	105.7	166.9±1.6	97.0	54.0±0.6	0.01±0.01	6dF J2132022-334254	323.009	-33.715	0.0293	Sy1	BG		
441	2MAXI J12131-334	322.9	-33.5	0.220	7.3	8.4±1.1	6.7	2.4±0.4	0.07±0.10	1RXS J213623.1-622400 (132)	324.096	-62.400	0.0588	Sy1	BG		
442	2MAXI J12136-624	324.1	-62.4	0.061	21.1	18.4±0.9	14.6	4.1±0.3	0.20±0.04								
443	2MAXI J12138-643	324.5	-64.3	0.122	10.9	9.6±0.9	9.6	2.5±0.3	0.10±0.07								
444	2MAXI J12144+383	326.2	38.4	<0.001	1171.9	6549.6±5.6	781.7	2176.6±2.8	-0.01±0.00	Cyg X-2 (133)	326.172	38.322		LMXB/NS	BG		
445	2MAXI J12147-693	326.8	-69.4	0.231	8.2	5.6±0.7	6.0	1.5±0.3	0.10±0.10								
446	2MAXI J12148-073	327.1	-7.4	0.191	8.1	8.8±1.1	5.3	1.9±0.4	0.21±0.11								
447	2MAXI J12148-166	327.2	-16.7	0.205	7.4	4.9±0.7	4.9	1.5±0.3	0.02±0.12								
448	2MAXI J12150+142	327.5	14.2	0.171	10.2	12.4±1.2	7.2	2.8±0.4	0.18±0.08								
449	2MAXI J12150-192	327.7	-19.2	0.113	11.7	12.1±1.0	11.4	3.6±0.3	0.04±0.06	6dF J2149581-185924	327.492	-18.990	0.1581	Sy1	B		
450	2MAXI J12151-723	327.8	-72.3	0.196	7.8	5.4±0.7	5.1	1.3±0.2	0.17±0.11								
451	2MAXI J12151-304	328.0	-30.5	0.099	12.7	15.3±1.2	10.8	3.9±0.4	0.12±0.06	PKS 2149-306	327.981	-30.465	2.345	Blazar	B		
452	2MAXI J12152-576	328.1	-57.7	0.088	14.7	13.4±0.9	13.8	4.3±0.3	0.01±0.05								
453	2MAXI J12154+778	328.7	17.8	0.108	12.1	14.7±1.2	11.2	4.3±0.4	0.06±0.06	RXC J2153.5+741	328.398	17.687	0.2329	Galaxy Cluster	M		
454	2MAXI J12157-061	329.5	-6.1	0.181	7.2	8.2±1.1	6.0	2.1±0.4	0.11±0.11	EUV J2157-06.1	329.363	-6.173		Star	B		
455	2MAXI J12200-600	330.2	-60.0	0.059	20.7	19.4±0.9	19.5	5.7±0.3	0.06±0.04	RXC J2201.9-5956 (134)	330.483	-59.949	0.098	Galaxy Cluster	MG		
456	2MAXI J12200+105	330.2	10.6	0.153	8.2	9.6±1.2	3.7	1.3±0.4	0.41±0.12	Mk 520	330.172	10.552	0.0266	Sy1.9	B		
457	2MAXI J12201-317	330.5	-31.8	0.065	20.8	25.2±1.2	6.4	2.2±0.4	0.57±0.05	NGC 7172 (135)	330.508	-31.870	0.0087	Sy2	BG		
458	2MAXI J12209-125	332.4	-12.5	0.107	11.9	13.4±1.1	12.4	4.2±0.3	0.02±0.06								
459	2MAXI J12213-891	333.3	-89.2	0.264	7.1	5.7±0.8	5.5	1.5±0.3	0.11±0.11								
460	2MAXI J12216-032	334.2	-3.3	0.131	11.0	12.5±1.1	10.6	3.9±0.4	0.03±0.07								
461	2MAXI J12216-647	334.2	-64.8	0.223	7.6	5.5±0.7	5.3	1.4±0.3	0.13±0.11	RXC J2218.0-6511	334.523	-65.185	0.0951	Galaxy Cluster	M		
462	2MAXI J12218-083	334.5	-8.4	0.047	28.3	33.6±1.2	10.4	3.7±0.4	0.49±0.04	FO AQR (137)	334.481	-8.351		CV/DQ Her	BG		
463	2MAXI J12218-388	334.7	-38.9	0.143	9.7	9.8±1.0	7.5	2.7±0.4	0.03±0.08	RXC J2218.6-3853	334.668	-38.898	0.1411	Galaxy Cluster	M		
464	2MAXI J12223-017	336.0	-1.8	0.089	12.7	14.7±1.2	8.9	3.2±0.4	0.20±0.07	RXC J2223.8-0138	335.970	-1.638	0.0906	Galaxy Cluster	M		
465	2MAXI J12225+912	336.5	1.2	0.194	7.1	8.4±1.2	4.2	1.5±0.4	0.29±0.13								
466	2MAXI J12235-259	338.8	-25.9	0.065	19.3	22.5±1.2	15.8	5.6±0.4	0.14±0.04								
467	2MAXI J12235-381	339.0	-38.1	0.152	13.9	14.0±1.0	11.4	4.3±0.4	0.03±0.06								
468	2MAXI J12238-126	339.6	-12.6	0.167	8.1	8.4±1.0	6.0	2.0±0.3	0.17±0.10	Mk 915	339.194	-12.545	0.0241	Sy1	B		
469	2MAXI J1241+297	340.5	29.7	0.148	7.5	8.4±1.1	12.0	4.5±0.4	-0.24±0.07								
470	2MAXI J12247-524	341.9	-52.5	0.096	13.3	14.0±1.1	12.0	4.0±0.3	0.07±0.06								
471	2MAXI J12249-641	342.4	-64.2	0.131	8.7	7.7±0.9	11.3	3.0±0.3	-0.08±0.07	RXC J2249.9-6425	342.488	-64.429	0.094	Galaxy Cluster	M		
472	2MAXI J12250-445	342.5	-44.6	0.163	8.9	11.9±1.3	8.7	3.4±0.4	0.06±0.08	RXC J2248.7-4431	342.181	-44.529	0.3475	Galaxy Cluster	M		
473	2MAXI J12252-323	343.2	-32.4	0.123	9.5	10.5±1.1	8.2	2.9±0.4	0.08±0.08								
474	2MAXI J12253+166	343.4	16.7	0.049	22.9	30.6±1.3	24.5	10.7±0.4	-0.03±0.03								
475	2MAXI J12254-174	343.5	-17.4	0.039	28.9	33.0±1.1	25.2	8.9±0.4	0.10±0.03	MR 2251-178 (140)	343.524	-17.582	0.064	Sy1	BG		
476	2MAXI J12255-030	343.8	-3.0	0.042	31.4	38.1±1.2	17.1	6.5±0.4	0.32±0.03								
477	2MAXI J12255-274	343.9	-27.4	0.216	7.2	8.1±1.1	4.6	1.6±0.3	0.24±0.12								
478	2MAXI J12300+250	345.0	25.0	0.156	9.7	10.1±1.0	6.7	2.4±0.4	0.16±0.09	KAZ 320	344.887	24.918	0.0345	Sy1	B		
479	2MAXI J12301-591	345.3	-59.1	0.177	8.3	8.8±0.8	4.5	1.2±0.3	0.29±0.12	2MASX J23013626-5913210	345.401	-59.222	0.149	Sy1	B		

TABLE 1 — CONTINUED

No.	Name	R.A.	Decl.	MAXI			(6)			(7)			(8)			(9)			(10)			(11)			Counterpart			(12)			(13)			(14)			(15)			(16)			(17)		
				(1)	(2)	(3)	(4)	(5)	(6)	(7)	(8)	(9)	(10)	(11)	(12)	(13)	(14)	(15)	(16)	(17)	(R.A.)	(Decl.)	(z)	Type ^[e]	Flag ^[f]	Note ^[g]																			
480	2MAXI J2303+086	345.8	8.7	0.071	17.8	21.7±1.2	16.9	6.6±0.4	0.03±0.04	NGC 7469	345.815	8.874	0.0163	Sy1.2	BM																														
481	2MAXI J2304-187	346.1	-18.8	0.177	7.0	7.4±1.1	4.5	1.5±0.3	0.25±0.12	PKS 2300-18	345.762	-18.690	0.1283	Sy1	B																														
482	2MAXI J2304-085	346.2	-8.6	0.040	31.3	38.0±1.2	27.1	10.5±0.4	0.09±0.02	Mk 926 (142)	346.181	-8.686	0.0469	Sy1.5	BG																														
483	2MAXI J2312-220	348.0	-22.1	0.131	9.6	10.3±1.1	9.0	3.0±0.3	0.05±0.08																																				
484	2MAXI J2316-424	349.1	-42.4	0.124	10.5	14.1±1.3	9.0	3.5±0.4	0.13±0.07																																				
485	2MAXI J2318+001	349.5	0.2	0.120	11.1	13.4±1.2	9.6	3.6±0.4	0.10±0.07	NGC 7603	349.736	0.244	0.0295	Sy1.5	B																														
486	2MAXI J2318+188	349.7	18.8	0.150	8.5	10.4±1.2	12.7	4.6±0.4	-0.15±0.07	RXC J2318.5+1842 (C)	349.612	18.724	0.0389	Galaxy Cluster	M																														
487	2MAXI J2319+421	349.9	42.1	0.142	9.4	12.5±1.3	8.9	3.9±0.4	0.03±0.08	RXC J2320.2+4146	350.060	41.779	0.14	Galaxy Cluster	M																														
488	2MAXI J2323+721	350.8	22.1	0.245	7.5	7.8±1.0	1.9	0.7±0.3	0.58±0.18																																				
489	2MAXI J2324+166	351.0	16.7	0.153	10.3	12.4±1.2	9.8	3.7±0.4	0.05±0.07	A2589	350.973	16.809	0.0416	Galaxy Cluster	M																														
490	2MAXI J2324-121	351.1	-12.1	0.111	11.4	11.3±1.0	11.7	4.1±0.4	-0.05±0.06	RXC J2325.3-1207	351.333	-12.127	0.0852	Galaxy Cluster	M																														
491	2MAXI J2330-022	352.7	-2.2	0.192	7.8	9.1±1.2	6.2	2.2±0.4	0.15±0.10																																				
492	2MAXI J2339-269	354.8	27.0	0.178	10.2	10.3±1.0	12.4	4.6±0.4	-0.16±0.06	RXC J2338.4+2659	354.607	27.012	0.0309	Galaxy Cluster	M																														
493	2MAXI J2344+092	356.2	9.3	0.110	10.3	12.5±1.2	12.7	4.9±0.4	-0.09±0.06	RXC J2344.9+0911	356.238	9.198	0.04	Galaxy Cluster	M																														
494	2MAXI J2348-280	357.1	-28.0	0.079	15.9	18.9±1.2	20.0	7.5±0.4	-0.09±0.04	RXC J2347.7-2808	356.930	-28.141	0.03	Galaxy Cluster	M																														
495	2MAXI J2354+286	358.6	28.6	0.119	10.3	12.4±1.2	13.8	5.3±0.4	-0.13±0.06																																				
496	2MAXI J2354-169	358.7	-16.9	0.156	9.1	8.9±1.0	6.1	2.0±0.3	0.18±0.10																																				
497	2MAXI J2356-106	359.2	-10.7	0.252	7.4	7.4±1.0	6.6	2.3±0.3	0.03±0.10																																				
498	2MAXI J2358-346	359.6	-34.7	0.105	13.4	15.7±1.2	16.5	6.3±0.4	-0.10±0.05																																				
499	2MAXI J2359-307	359.8	-30.8	0.121	10.2	11.7±1.1	9.9	3.5±0.4	0.04±0.07	H 2356-309	359.783	-30.628	0.1651	BL Lac	B																														
500	2MAXI J2359-068	359.9	-6.8	0.195	7.1	7.5±1.1	4.2	1.5±0.4	0.23±0.13	2MASX J00004876-0709117	0.203	-7.153		Galaxy	B																														

^a The 1 σ statistical position error in units of degree. There exists an additional systematic error of $\approx 0.09^\circ$ (90%). See section 4.4 for details.

^b The observed 4-10 keV flux in units of 10^{-12} ergs cm $^{-2}$ s $^{-1}$, converted from Crab units by assuming the Crab-like spectrum; 1 mCrab = 1.21×10^{-11} ergs cm $^{-2}$ s $^{-1}$.

^c The observed 3-4 keV flux in units of 10^{-12} ergs cm $^{-2}$ s $^{-1}$, converted from Crab units by assuming the Crab-like spectrum; 1 mCrab = 3.98×10^{-12} ergs cm $^{-2}$ s $^{-1}$.

^d The numbers in parentheses represent source identification ones in the GSC7 catalog.

^e Sy: Seyfert galaxy, L(HMXB): low/high-mass X-ray binary, Symb: symbiotic star, WD: white dwarf, NS: neutron star, BH: black hole candidate, CV: cataclysmic variable, msPSR: millisecond pulsar, FSRQ: flat-spectrum radio quasar

^f Cross-matching flag; B, M, and G represent that the source has more one or more counterparts in the BAT70, MCXC, and GSC7 catalog, respectively. The counterpart name listed in column (11) is quoted from the catalog expressed by the leftmost letter in this column.

^g (A) We change the counterpart name from SWIFT J0042.7-4111 to M31 taking into account the angular resolution of MAXI/GSC. (B) RXC J0105.5-2439 is another counterpart of this source. (C) We change the counterpart name from CXO J051406.4-400238 to NGC 1851 taking into account the angular resolution of MAXI/GSC. (E) Since NGC 1275 to Perseus Cluster taking into account the angular resolution of MAXI/GSC. (D) We change the counterpart name from CXO J051406.4-400238 to NGC 1851 taking into account the angular resolution of MAXI/GSC. (F) Since the position accuracy of 3EG J1627-2419, the counterpart of MAXI J0957+693 is a confused source consisting of M81, M82, and RXS J095755.0+69310, we use the position determined by the MAXI/GSC 7-month survey for the cross-matching. (G) ESO 139-G 012 is another counterpart of this source.